Fermi National Accelerator Laboratory

AN EXPERIMENTAL STUDY OF MULTIPARTICLE PRODUCTION

IN HADRON-NUCLEUS INTERACTIONS AT HIGH ENERGY

J. E. Elias
Fermi National Accelerator Laboratory
Batavia, Illinois 60510

and

W. Busza, C. Halliwell, D. Luckey,
P. Swartz, L. Votta, and C. Young
Massachusetts Institute of Technology
Cambridge, Massachusetts 02139

June 1979

AN EXPERIMENTAL STUDY OF MULTIPARTICLE PRODUCTION

IN HADRON-NUCLEUS INTERACTIONS AT HIGH ENERGY[*]

J. E. Elias
Fermi National Accelerator Laboratory
Batavia, Illinois 60510

and

W. Busza, C. Halliwell, D. Luckey,
P. Swartz,[§] L. Votta, and C. Young[+]
Massachusetts Institute of Technology
Cambridge, Massachusetts 02139

ABSTRACT

Hadron-nucleus interactions have been studied in the 50 to 200 GeV/c momentum range for incident pions, kaons, protons and antiprotons. Average charged multiplicities, dispersions of multiplicity distributions, inelastic cross sections and angular distributions are presented. The energy dependence of the target and projectile fragmentation regions is studied in detail.

I. INTRODUCTION

Hadron-nucleus interactions have been studied extensively in recent years.[1] For incoherent interactions, the multiplicity of charged particles does not depend strongly on the atomic number A, or the incident particle type. In addition, the mean multiplicity has a weak-energy dependence, similar to that seen in pp collisions. The lack of significant nuclear cascading has led to the conclusion that the high energy secondaries produced in the fundamental hadron-nucleon collision take a long time to form compared to nuclear dimensions.

Theoretical attempts to interpret the detailed features of hadron-nucleus data have depended on using data from several different experiments. Until this experiment the effects of incident projectile types, incident energy, and target species have not been studied using the same apparatus. Pions, kaons, and protons of both polarities with momenta ranging from 50 to 200 GeV/c were incident on targets ranging from beryllium to uranium. Absorption cross-sections, charged particle multiplicities and angular distributions were measured. It is hoped that strong constraints can be applied to theoretical models because of the systematic consistency of these measurements.

Earlier publications have reported on specific results of this experiment.[2] Detailed descriptions of the apparatus, data collection procedure, analyses and corrections are given in Sections II, III and IV. Tabular listings of all the results and consistency

checks are presented in Section V. Comparisons with other experiments and a discussion of results are given in Sections VI and VII, followed by general conclusions in Section VIII.

II. EXPERIMENTAL APPARATUS AND PROCEDURES

The experiment was performed at Fermilab using the M6 unseparated charged beam in the Meson Laboratory. Two sets of measurements were made which will be referred to as Part I and Part II in the following discussions. In Part I, the general features of hadron-nucleus interactions were studied by measuring nuclear absorption cross sections and average charged multiplicities using an untagged negative beam at 100 and 175 GeV/c. A more detailed study was carried out in Part II. In addition to measuring the angular distributions of secondaries with an augmented detector, the projectile dependence was investigated using Cerenkov counters to identify incident particles of both signs in the momentum range 50 to 200 GeV/c. For both parts of the experiment a lead radiator was installed at an upstream focus to remove electrons from the beam.

A. Part I - Apparatus

The apparatus, shown schematically in Fig. 1, was placed at the second focus of the beam line. A scintillation counter telescope consisting of trigger counters T1 and T2 with hole counters V1 and V2 in veto defined the incident particle trajectory. The

pulse height in T1 was required to be less than 1.5 times minimum ionizing to decrease the possibility of more than one particle arriving within the resolution time of the trigger. In addition, successive incident particles were required to be separated in time by at least 150 nsec because of the slow response time of the detection apparatus.

The data acquisition system was triggered by an inelastic interaction indicated by the presence of one or more wide-angle secondaries or more than one forward particle. Counters $dE/d\bar{x}_1$ and dE/dx_2 were used with 1.5 times minimum ionizing thresholds for forward particles, and hole counters W_1 and W_2 intercepted wide-angle tracks. A 2 cm thick aluminum plate shielding W_2 reduced the trigger rate from -rays. The trigger was a three-fold coincidence between the beam trigger, the inclusive OR of dE/dx_1 and W_1, and the inclusive OR of dE/dx_2 and W_2. Finally, a third beam trigger counter, V_3, placed on the downstream beam trajectory after a series of dipole magnets was added in anticoincidence to further reduce spurious triggers.

Since the incident particles were not identified, only negative particles were used to maximize the pion component. The hadron composition of the beam[3] was 93.8% pions, 4.1% kaons, and 2.1% antiprotons at 100 GeV/c, and 96.2% pions, 3.4% kaons, and 0.4% antiprotons at 175 GeV/c. At both momenta, the muon component amounted to approximately 1% of the hadron component.

The multiplicity detector, as shown in Fig. 1, consisted of 13 counters. Twelve counters formed a truncated cone with the axis

along the incident beam direction. These 12 elements were made of ultra violet transmitting (UVT) lucite. A 1/2" carbon layer, which absorbed low-energy δ-rays, lined the inside upstream face of the cone. The 13th counter, labeled "C" in Fig. 1, was a 12-sided bevelled slab of UVT lucite which fitted into the hole of the truncated cone.

All 13 counters were designed to detect only relativistic particles. As shown in Fig. 2, UVT lucite emits substantial Cerenkov light only for particles with velocities greater than approximately 0.85 c. Therefore, slow secondaries such as nuclear fragments would not be detected in these counters. From Fig. 2 it is also apparent that for highly relativistic particles ($\gamma \geq 3$) the light output from UVT lucite is constant, regardless of the particle momentum. This property was used to count the number of relativistic secondaries traversing the forward-looking "C" counter by means of pulse height. A typical pulse-height spectrum resulting from hadron-aluminum interactions is shown in Fig. 3.

B. Part II - Apparatus

In Part II, the experiment was moved downstream of the M6 beam line Cerenkov counters so that particle identification on an event-by-event basis could be used. Figure 4a shows the layout of the beam line trigger and veto counters. Requirements similar to those used in Part I were imposed on the separation between successive incident particles. However, downstream dipole magnets were not present at this location to isolate the interaction region from the final veto counter V3. Thus V3 was not used in the trigger but was recorded for subsequent analysis.

The detection apparatus was augmented as diagrammed in Fig. 4b in order to measure the angular distribution of secondaries. The 12 element cone-shaped hodoscope was separated from the forward-looking "C" counter by approximately 1.2 meters, and three ring-shaped hodoscopes were placed in the intervening space. Each ring hodoscope consisted of two layers of six counters; each counter subtended 60° of the azimuth with the layers rotated by 30° relative to one another. The upstream layer was made of 3/4" UVT lucite; the downstream one of 1/4" scintillator. The lucite imposed a velocity selection of $\beta \geq 0.85$, and also served as a δ-ray absorber so that only the most energetic δ-rays would penetrate to the scintillator layer.

As in Part I, the data acquisition system was triggered by an inelastic interaction signaled by the presence of wide-angle secondaries or more than one forward particle. The three ring hodoscopes were used to detect wide-angle secondaries by requiring a coincidence between both layers of a given ring. The two dE/dx counters with 1.5 times minimum ionizing thresholds were used in coincidence to detect forward secondaries. Thus the trigger consisted of the inclusive OR of the above two systems in coincidence with a beam trigger.

C. Experimental Procedure

In both parts of the experiment, data were collected with the apparatus placed in several configurations. By moving the target with respect to the multiplicity detector and by varying the relative positions of the separate parts of the detector, several

different configurations for the angular acceptance were obtained. A summary of these acceptances in terms of both the laboratory polar angle θ_L and pseudorapidity $\eta = -\ln(\tan(\theta_L/2))$, is shown in Fig. 5. The limits on the acceptance were defined by the downstream veto counter in the forward region and the upstream edge of the 12-element hodoscope in the wide-angle region.

Data were taken for several thicknesses of each target material listed in Table 1 to allow an extrapolation of the results to zero thickness. Target lengths ranged from 0.5% to 5% of an absorption length for carbon (0.01 to 0.1 radiation lengths) to 0.1% to 1% of an absorption length for lead (0.03 to 0.3 radiation lengths). Hydrogen results were acquired by a polyethylene-carbon subtraction.

III. ANALYSIS

In Part I of the experiment, pulse height information from the "C" counter was digitized and accumulated in a pulse-height analyzer. Eight independent spectra were collected simultaneously depending on the number of slats that had fired in the wide-angle hodoscope. When 7 or more of the 12 slats fired, the corresponding pulse height information was added to the eighth spectrum. Thus, the data record consisted of eight integrated pulse height spectra and corresponding flux scaler information.

Since the objective of Part II was to measure the angular distributions of secondaries, "C" counter pulse height information

was collected on an event-by-event basis using a PDP-11/10 computer. In addition, the status of the 36 ring-hodoscope slats, 12 wide-angle slats, beam veto counter V3, and 3 particle identifying beam Cerenkov counters was recorded for each event.

The first stage of the analysis removed events with low total multiplicities; $\leq$ 3 charged relativistic particles for Part I, $\leq$ 2 for Part II. The clear separation of 1, 2, and 3-particle peaks in the "C" counter pulse height spectrum (Fig. 3) enabled this to be accomplished. This cut eliminated a large fraction of the triggers caused by single δ-ray production in the target, beam particles which gave large pulse heights in both dE/dx_1 and dE/dx_2, and elastic collisions. Next, empty target contributions corresponding to $\sim 0.2\%$ of an interaction length were subtracted for each run. Part II data had an additional requirement of unambiguous beam-particle identification, and the downstream veto counter requirement was implemented in software. Interaction rates at this stage of the analysis required a multiplicity-dependent correction, described later, for the loss of inelastic events resulting from the low multiplicity cut before cross sections could be determined.

In the second stage of the analysis, the average multiplicities detected by each part of the apparatus were determined. The different methods used for the "C" counter, wide-angle hodoscope and ring hodoscopes are described below.

A) "C" Cerenkov Counter

The average multiplicity n_c corresponding to a "C" counter pulse height distribution was computed from the mean pulse height $<x>$ as

$$n_c = \langle x \rangle / \langle x_1 \rangle$$

where $\langle x_1 \rangle$ is the average pulse height of a single particle spectrum. This simple relation is true so long as the n-particle response is a simple n-fold convolution of the single particle response.[*]

Similarly, the dispersion of the multiplicity distribution D_c was computed from the dispersion of the pulse height spectrum D as:

$$D_c^2 = \left(D^2 - n_c D_1^2\right) / \langle x_1 \rangle^2$$

where D_1 is the dispersion of the one particle spectrum.

B) Wide-Angle Hodoscope

Although the number of fired elements was known directly there was no attempt to detect multiple hits within a given element. Therefore, it was necessary to adjust the observed multiplicity for such occurrences. Assuming no azimuthal correlations between secondaries, the probability $P(r,n)$ of n secondaries hitting r out of a total of 12 counters is[*]:

$$P(r,n) = \frac{12!}{(12-r)! \; 12^n} \sum_{j=0}^{r-1} \frac{(-1)^j \; (r-j)^n}{(r-j)! \, j!}$$

The product of the inverse of the above matrix and the observed multiplicity distribution resulted in the final distribution. The mean and dispersion of this distribution were then calculated

directly. In the above equation, r and n range independently from 1 to 7 for Part I and from 1 to 12 for Part II.

C) Ring Hodoscopes

As mentioned previously, each ring hodoscope defined 12 distinct equal-size azimuthal bins. Consequently, one out of a total of 2^{12} possible outcomes occurred for any given event. By invoking rotational symmetry this number is reduced to 322. Assuming no azimuthal correlations, the number of independent combinations can be further reduced to 73.

The frequency distributions over the 322 possible patterns for uncorrelated n-prong events were calculated for each n separately. The effects of low energy δ-rays were determined similarly assuming no penetration to the back scintillator layer. On the other hand, γ-rays which converted into electron pairs deep in the lucite layer would be detected only in the downstream scintillator layer. This effect was also taken into account.

The experimentally observed 322 bin frequency vector from each ring was fitted to a linear superposition of the generated event vectors described above. The maximum multiplicity of these generated vectors was increased until both the average fitted multiplicity and chi-squared per degree of freedom became constant. For statistically poorer data (e.g., kaon-induced events) lack of azimuthal correlations was assumed for the data and the frequency vectors were reduced to 73 bins. The validity of this procedure was checked by studying high statistics proton-induced data. The results of the two methods were indistinguishable.

The third stage of the analysis consisted of combining infor-
mation from the separate parts of the detector. The mean total
multiplicity was determined by adding average multiplicity results
from the individual parts of the detector. The ring-hodoscope
analysis did not permit a straightforward determination of the
dispersion of the total multiplicity distribution. Hence,
dispersion information was obtained only from Part I data.

IV. CORRECTIONS TO THE DATA

Various corrections were then applied to obtain the final
cross sections, multiplicities, and angular distributions.

A) Cross Sections

Absorption cross sections for π^--nucleus collisions were
determined using the data from Part I. Coherent and elastic events
were eliminated by removing the low multiplicity events in the
first stage of the analysis. Estimates for the loss of low multi-
plicity incoherent events were made by assuming that the
multiplicity distribution had the form $n^3 e^{-\lambda n}$, with the high-multi-
plicity data providing a rough determination of λ. As low-multi-
plicity events are a small contribution to hadron-nucleus inelastic
cross sections ranging from -20% in 40 GeV/c π^--carbon collisions,[4]
down to -8% in 200 GeV/c π^--emulsion collisions.[8] Systematic errors
introduced by this procedure were estimated to contribute less than
5%.

Cross sections were further corrected for muon contamination
in the beam by renormalizing the incident flux. The effects of the

small K^- and $\bar{p}$ contamination were calculated by estimating their absorption cross sections. The total correction arising from the untagged beam was typically 3%.

B) Angular Distributions

The method used to determine the average number of secondaries from low-multiplicity events for Part I has been described above. In Part II the number of such events was estimated using the cross sections measured in Part I and Ref. 7. Assuming an average multiplicity of 1.25, the effect of the low-multiplicity cut was included in the angular distributions as an overall normalization correction. Changing the assumed multiplicity from 1.25 to 0.75 varied this normalization by ~2%. In order to estimate the systematic bias resulting from this procedure, a sample of hydrogen bubble chamber data[*] was analyzed identically. A 3% effect was seen in the hodoscope multiplicities and ~10% effect in the "C" counter. Consequently no angle-dependent corrections were applied to the distributions.

Multiplicities from the wide-angle hodoscope were increased by ~5% to correct for the cracks between adjacent elements. No correction was applied for interactions within an element; it was assumed that the resulting secondaries would be contained within that element.

The analysis of the "C" counter spectra required knowledge of the average pulse height from a single relativistic particle. Non-interacting beam particles were used for this calibration. Hadronic interactions of such a particle in the counter's radiator

would affect the average pulse height. This effect was smaller for secondaries due to their lower momenta. On the other hand, e^+e^- pairs from π^0 decay photons cause an increase in pulse height leading to an apparently higher multiplicity. The combined correction for these competing effects were estimated, and the observed multiplicity lowered by 3%.

Finally, the average multiplicities in each detector were linearly extrapolated to zero target thickness. This corrected for extra-nuclear cascades, conversion of γ-rays from π^0's in the target, and production of hard δ-rays.

V. RESULTS

The results from Part I consist of absorption cross sections, coarse angular distributions, and multiplicity dispersions. The average of the 100 and 175 GeV/c π^- absorption cross sections are summarized in Table 2. All systematic and statistical uncertainties are included in the errors. Angular distributions are listed in Tables 3 and 4 along with total multiplicities and dispersions.

In Part II, data at all 3 detector configurations (see Fig. 5) were acquired for only a few of the 12 target materials studied. For these targets, angular distributions were obtained directly by averaging over the 3 geometries, and the results are tabulated in Table 5. The errors do not include uncertainties introduced by the low multiplicity corrections and the averaging over different geometries. Their combined effects are estimated to be ~3%.

Multiplicity data from the remaining targets were combined with these results to generate a parameterized form of the target dependence of the angular distribution. The form of the parameterization chosen was a polynomial in $\bar{v}$ where $\bar{v}$ is a measure of the average amount of nuclear material involved in an inelastic interaction. The parameter $\bar{v}$ is given by:

$$\bar{v} = \frac{A\sigma_N}{\sigma_A}$$

where σ_N is the hadron-nucleon absorption cross section and σ_A is the corresponding hadron-nucleus cross section. Thus $\bar{v}$ is the average number of inelastic collisions that the incident hadron would undergo in traversing the nucleus assuming that all collisions are governed by the cross section of the incident hadron.

A further understanding of the parameter $\bar{v}$ is provided by considering a simple model in which a nucleus with atomic number A is assumed to have a density distribution (b,z). The probability for a hadron incident along the z-axis at impact parameter b having v collisions is

$$P(v) = \frac{1}{v!} \int_{-\infty}^{\infty} (\sigma_N \ell)^v \, e^{-\sigma_N \ell} \, d^2b$$

where

$$\ell = \int_{-\infty}^{\infty} \rho(b,z)dz$$

The absorption cross section for the hadron-nucleus interaction is
then

$$\sigma_A = \int_{-\infty}^{\infty} (1-e^{-\sigma_N L}) \, d^2b$$

and the average number of collisions $\bar{\nu}$ is

$$\bar{\nu} = \frac{A\sigma_N}{\sigma_A}$$

It is emphasized that $\bar{\nu}$ depends not only on the type of nucleus
being considered, but also on the incident hadron. Figure 6 shows
typical $P(\nu)$ distributions calculated using a Wood-Saxon form for
the distribution of nuclear matter.[9]

The results obtained from this overall parameterization of the
target dependence of the angular distributions are listed in Table
6. Since the polynomial coefficients are correlated, fractional
errors on the number of secondaries at integer values of $\bar{\nu}$ are given
instead of coefficient uncertainties. The errors quoted do not
include possible systematic biases arising from the use of a poly-
nomial form in $\bar{\nu}$ to fit the data.

The values of $\bar{\nu}$ used in this analysis were calculated by using
experimentally measured hadron-nucleus cross sections at 25–60
GeV/c[7] and hadron-proton data from Ref. 3. Corrections for the
energy dependence of $\bar{\nu}$ were calculated using the multiple-scatter-
ing model mentioned above. The resulting $\bar{\nu}$ values for different
projectiles and energies were fitted to the form kA^c for $A > 1$, and
results are listed in Table 7.

In order to compare the total charged multiplicity results determined in the two parts of this experiment, several conversion factors must be applied to the Part I results. An acceptance factor was needed as $\theta_L \leq 110^o$ for Part I and $\theta_L \leq 126^o$ for Part II. At 100 GeV/c, allowance for the different incident particle types, π^+ and π^-, between the two parts was necessary, and at 175 GeV/c an incident momentum factor was required to compare with the Part II 200 GeV/c results. Finally, an analysis factor was needed for the wide-angle hodoscope information as analyzing Part II data identically to Part I resulted in a systematic decrease in multiplicity of 5% for heavy targets. The results of this comparison are given in Table 8 along with a list of the conversion factors used. Except for uranium, the two parts of the experiment gave consistent results. Total multiplicities obtained in Part II are preferred because the equipment was capable of resolving higher multiplicities in the wide-angle hodoscope and had larger acceptance.

VI. COMPARISON OF RESULTS WITH OTHER EXPERIMENTS

The nuclear absorption cross sections obtained from Part I are compared with 60 GeV/c and 200 GeV/c data[7] in Table 2. In Table 9 multiplicities and dispersions for π^-p interactions and bubble chamber experiments are compared.[10,11,12] In Table 10 a comparison between $\bar{\nu} = 1$ multiplicities (see Table 6) from Part II of this experiment and bubble chamber data[13] is shown. It is estimated that the velocity requirement of $\beta \geq 0.85$ decreases the total multiplicity measured in this experiment by ~ 0.5.[14]

Figure 7 compares 100 GeV/c hadron-proton rapidity distributions $N(\Delta y)/\Delta y$'s with pseudorapidity distributions $N(\Delta\eta)/\Delta\eta$ from this experiment. A systematic effect is evident. The pseudorapidity distributions of this experiment are shifted by _0.3 units with respect to the rapidity distributions. This is primarily due to the fact that out of necessity distributions in different variables have been used in the comparison. Figure 8 shows that when bubble chamber data are analyzed in an identical way to data from this experiment excellent agreement is achieved.

The CH_2-C data obtained from this experiment satisfactorily reproduce the trends seen previously in bubble chamber data. However, they are not as precise as the compiled world data for hadron-proton interactions.[15] Thus in subsequent calculations involving total charged hydrogen multiplicities the latter, (with 0.5 particles subtracted) are used.

Figure 9 shows pseudorapidity distributions obtained from 200 GeV emulsion exposures.[16,17] They are compared with results of this experiment. The value of $\bar{v}$ is 2.39 for a proton-emulsion interaction and is 2.06 for a pion-emulsion interaction. Similar comparisons of total multiplicities[16,18,19,20] at various energies are given in Table 11.

The angular distributions are also compared with data from neutron-nucleus interactions. Figure 10 shows a comparison of the atomic number dependence of the inclusive cross section $\sigma(\Delta\eta)/\Delta\eta$ from this experiment with that from Ref. 21. Figure 11 is a comparison of the pseudorapidity distributions from neutron-induced

interactions in beryllium, copper, and lead[22] with those initiated by protons in this experiment.

VII. DISCUSSION OF RESULTS

A. Total Multiplicities

From Table 5 it is evident that the total multiplicities from nuclear targets increase slowly with nuclear thickness and incident energies. This is consistent with a slow evolution of the asymptotic state from a hadron-nucleon collision. A measure of the multiplication that does occur is given by the ratio of the hadron-nucleus multiplicities, $<n>_{hA}$, from Table 5 to the corresponding hadron-nucleon multiplicities $<n>_{hp}$ from Table 10. The $\bar{\nu}$ dependence of this ratio, R_A, is shown in Fig. 12. Effects of the errors on $<n>_{hp}$ are not included. It is apparent that the effect of the incident hadron's identity is entirely accommodated by the use of the variable $\bar{\nu}$ to describe nuclear thicknesses.

The hypothesis that all collisions other than the first are governed by the cross section of a pion rather than that of the incident hadron[23] can be examined with the parameter $\bar{\nu}'$. It is the average number of inelastic collisions that the incident hadron h would undergo in traversing the nucleus, assuming that, while the initial collision is governed by the cross section of the incident hadron, all subsequent collisions are governed by the pion cross section. The values of $\bar{\nu}'$ are given by the formula:

$$\bar{\nu}' = 1 + (\bar{\nu}-1)\ \frac{\sigma_{\pi p}}{\sigma_{hp}}$$

The multiplicity ratio R_A is plotted versus $\bar{\nu}'$ for 50 and 100 GeV/c incident particles in Fig. 13. The universal behavior observed earlier is no longer evident.

It could be argued that for this comparison, $<n>_{\pi p}$ or some weighted average of $<n>_{hp}$ and $<n>_{\pi p}$, rather than $<n>_{hp}$, should be used in the denominator of the scaled multiplicity. This would in fact make little difference. For example, R_A for lead would be changed by only -10% if $<n>_{\pi p}$ rather than $<n>_{pp}$ were used, while $\bar{\nu}'$ would differ from $\bar{\nu}$ by - 30%. Consequently a large effect would remain.

Scaled total multiplicities are adequately described by a linear relationship between R_A and $\bar{\nu}$. It can be seen from Fig. 14 that these data are not precise enough to differentiate between unconstrained fits and ones which are required to pass through the hadron-proton point (R_A = 1, $\bar{\nu}$ = 1). Fit parameters are summarized in Table 12 a. No energy dependence of the parameters is evident. This can also be seen from Fig. 15 where scaled multiplicities from three nuclear targets show no variation within the energy range of this experiment.

The results of using an alternative form for the parameterization of the scaled multiplicities, R_A vs. A^β, are shown in Table 12 b. Fits are good for data obtained with a unique type of beam projectile. However, there is no adequate universal fit.

B. Dispersion of Multiplicity Distribution

Figure 16 shows that the relationship between the dispersion and the average of the multiplicity distribution is similar in π^--nucleus interactions, $D = (0.54 \pm 0.16) <n> - (0.59 \pm 0.02)$, and π^--proton interactions,[24] $D = 0.56<n> - 0.58$.

C. Angular Distributions

Differential multiplicities, $N(\Delta\eta)/\Delta\eta$ from the 12 angular regions were separately fitted to the form $A^{\alpha'(\eta)}$ in order to look for possible intranuclear cascading. The results of these fits are displayed in Fig. 17 for the various momenta and projectiles. Since this angular distribution is proportional to the differential inelastic cross section normalized by the total absorption cross section, the A-dependence of the differential cross section can be extracted as

$$\alpha(\eta) = \alpha'(\eta) + \gamma$$

where γ describes the A-dependence of the total cross section. Using $\gamma = 0.69$, 0.77, and 0.75 for protons, kaons, and pions, respectively,[7] the results in Fig. 17 show that $\alpha(\eta)$ becomes greater than unity in the region $\eta \leq 1.5$ indicating that cascading within the nucleus is taking place.

The region of cascading does not appear to depend on incident particle type or incident momentum. All data in the forward region approach $\alpha' = 0$. There is no evidence of $\alpha'(\eta)$ becoming negative. This is in agreement with data from the neutron-nucleus data shown

in Fig. 10, but contradicts that which has been concluded from π^- and p-emulsion exposures.[18,23] As the incident momentum is varied from 50 to 200 GeV/c, the value of α' increases for all $\eta \geq 1.5$.

The increase with energy of the dispersion of the angular distribution is weakly dependent on nuclear thickness and is approximately equal to the increase in kinematical phase-space. Angular distributions shown in Fig. 18 for various incident momenta illustrate these effects.

A detailed study of the projectile fragmentation region can be achieved by boosting the laboratory frame to the rest frame of the incident projectile. There is no unique transformation for the pseudorapidity variable, η. Consequently, the rapidity boost, $1/2(\ln (2p/m))$, where p and m are the incident projectile's momentum and mass, has been employed. Figure 19 shows the result of performing this boost on data for incident protons. The energy-independent region, in this frame, extends over ~ 5 units of pseudorapidity for the lead data reducing to ~ 4 units for the carbon data.[26] The energy-independent region for nucleon data is also shown. Figure 20 shows that the energy-independent region is maintained over the same range of pseudorapidity regardless of incident particle type; $\bar{\nu} = 1$ data from·this experiment are also shown and are consistent with the lead data over 3 units of η. In the target fragmentation region, multiplicities from different incident energies are consistent over ~ 3 units of η, but there is no agreement with hydrogen data due to cascading within the nucleus.

Comparing pion-induced data with proton-induced data shows, once again, that R_A scales with $\bar{\nu}$. From Fig. 21 it can be seen that

by boosting pion and proton data by the same amount, multiplicities from identical targets (in this case, lead) are not consistent. However, when scaled multiplicities from targets with the same $\bar{\nu}$ are compared, consistency results.

Multiplicity distributions over the total angular range are shown in Fig. 22 for various nuclear thicknesses. The movement of the peak of the distribution to larger angles as nuclear thickness increases has been interpreted as evidence for collective effects within the nucleus.[27]

It has been proposed[28] that the multiplicity in the central region should eventually saturate for very thick nuclei. In Fig. 23 multiplicities from the region of laboratory rapidity corresponding to the incident hadron-nucleon system have been plotted. Although some curvature appears to be present, no definitive statement, within the statistical accuracy of this experiment, can be made.

VIII. CONCLUSIONS

A detailed study of multiparticle production in hadron-nucleus interactions has shown:

1) Average charged multiplicities can be parameterized in terms of a universal dependence on the thickness of a nucleus as measured by the absorption mean free path of the incident hadron. This dependence is independent of the energy and the identity of the incident particle.

2) The relation between the dispersion of the multiplicity distribution in pion-nucleus interactions and its mean is the same as that observed in pion-nucleon interactions.

3) The multiplicity of charged secondaries is independent of incident momentum in two angular regions; one, the wide-angle region, occupies approximately 3 units of pseudorapidity. The other, the forward region, occupies a larger range of pseudorapidity, varying from -3 units for pp collisions to -5 units for pPb collisions.

4) The multiplicity in the very forward region ($\eta \geq 4.0$) is also independent of nuclear thickness.

ACKNOWLEDGMENTS

REFERENCES

[1]For recent experimental reviews on various aspects of hadron-nucleus interactions see:

    i) I. Otterlund, Acta Phys. Polon. B8, 119 (1977);

    ii) W. Busza, Acta Phys. Polon. B8, 333 (1977);

    iii) C. Halliwell, Proceedings of the VII International Colloquium on Multiparticle Reactions, Kaysersburg, June 1977; R. Arnold, J. Gerber, and P. Schubelin, ed. (Centre de Recherches Nucleaires, 1977).

    iv) T. Ferbel, Proceedings of the XIX International Conference on High Energy Physics, Tokyo, 1978 (to be published).

[2]W. Busza et al., Phys. Rev. Lett. 34, 836 (1975);

C. Halliwell et al., Phys. Rev. Lett. 39, 1499 (1977);

J. E. Elias et al., Phys. Rev. Lett. 41, 285 (1978).

[3]D. S. Ayres et al., Phys. Rev. D15, 3105 (1977).

[4]C. Young, Ph.D. Thesis, M.I.T., 1977 (unpublished).

[5]S. A. Azimov et al., Nucl. Phys. B107, 45 (1976).

[6]Z. V. Anzon et al., Nucl. Phys. B129, 205 (1977).

[7]S. P. Denisov et al., Nucl. Phys. B61, 62 (1973);

A. S. Carroll et al., Phys. Lett. 80B, 319 (1979).

[8]Michigan-Rochester 100 GeV pp bubble chamber exposure (T. Ferbel, private communication.)

[9]J. W. Negele, Phys. Rev. C1, 1260 (1970).

[10]E. L. Berger et al., Nucl. Phys. B77, 365 (1974).

[11]D. Fong et al., Phys. Rev. Lett. 37, 736 (1976).

[12]D. Bogert et al., Phys. Rev. Lett. 31, 1271 (1973).

[13] J. Whitmore, Phys. Rep. $\underline{27C}$, 187 (1976).

[14] G. Calucci et al., Phys. Rev. $\underline{D10}$, 1468 (1974).

[15] W. M. Morse et al., Phys. Rev. $\underline{D15}$, 66 (1977).

[16] B. Furmanska et al., Acta Phys. Polon. $\underline{B8}$, 973 (1977).

[17] B. Andersson et al., Lund University Preprint LU TP 77-16, 1977 (Unpublished).

[18] S. A. Azimov et al., in the Proceedings of "Multiparticle Production on Nuclei at Very High Energies," IAEA-SMR-21, ICTP, 1977; G. Bellini et al., ed.

[19] I. Otterlund, Ref. 1.

[20] I. Otterlund, op. cit. Ref. 18.

[21] D. Chaney et al., Phys. Rev. Lett. $\underline{40}$, 71 (1978).

[22] D. L. Burke et al., University of Michigan Preprint UM-HE-78-6 1978 (Unpublished).

[23] Such a hypothesis is based on the argument that since the asymptotic state is predominantly pions, the immediate product of a hadron-nucleon interaction may have properties more similar to those of a pion than to those of the incident particle.

[24] E. de Wolf et al., Nucl. Phys. $\underline{B87}$, 325 (1975).

[25] E. G. Boos et al., Nucl. Phys. $\underline{B143}$, 232 (1978).

[26] The kinematical limits on η are $-\infty$ to ∞. For this discussion the limits on rapidity, y, (e.g., -1.9 to 8.0 for pions produced in 200 GeV pp collisions) are used instead. This is justified by the fact that very few secondaries are outside the range $y_{min} > \eta > y_{max}$ (see Fig. 9).

[27] Y. Afek et al., op. cit. Ref. 18.

[28] A. Bialas et al., Acta Phys. Polon. $\underline{B8}$, 585 (1977).

Table 1. Summary of types of targets used for various
incident particles. xxx signifies data collected.

Incident Particle Momentum (GeV/c)	Particle Type	Part 1 or Part 2	Target Type											
			Be	C	CH_2	Al	Ti	Cu	Mo	Ag	W	Pb	U	Emul-sion
50	π^+	2		xxx	xxx			xxx		xxx		xxx		
50	K^+	2		xxx	xxx			xxx		xxx		xxx		
50	p	2		xxx	xxx			xxx		xxx		xxx		
100	π^-	1		xxx	xxx	xxx		xxx		xxx		xxx	xxx	xxx
100	π^+	2	xxx	xxx	xxx	xxx	xxx	xxx		xxx		xxx	xxx	xxx
100	K^+	2	xxx	xxx	xxx	xxx	xxx	xxx		xxx		xxx	xxx	xxx
100	p	2	xxx	xxx	xxx	xxx	xxx	xxx		xxx		xxx	xxx	xxx
175	π^-	1		xxx	xxx			xxx				xxx		
200	π^+	2	xxx	xxx	xxx	xxx	xxx	xxx	xxx	xxx	xxx	xxx	xxx	xxx
200	π^-	2	xxx	xxx	xxx	xxx		xxx		xxx		xxx	xxx	xxx
200	p	2	xxx	xxx	xxx	xxx	xxx	xxx	xxx	xxx	xxx	xxx	xxx	xxx
200	$\bar{p}$	2	xxx	xxx	xxx	xxx	xxx	xxx	xxx	xxx	xxx	xxx	xxx	xxx

Table 2.   Comparison of π^--nucleus absorption cross
sections from this experiment (average of
100 and 175 GeV/c results) with measure-
ments at 60 GeV/c (S.P. Denisov et al. Ref. 7)
and 60 and 200 GeV/c (A.S. Carroll et al.,
Ref. 7).   Cross sections are measured in
millibarns.

Element	σ (This Exper.)	$\sigma(60)$	$\sigma(60)$	$\sigma(200)$
C	172 ± 10	182 ± 3	169 ± 5	170 ± 5
Al	320 ± 25	340 ± 4	324 ± 10	325 ± 10
Cu	650 ± 25	654 ± 15	625 ± 19	625 ± 19
Pb	1470 ± 70	1510 ± 25	1478 ± 44	1467 ± 44
U	1750 ±100	1775 ± 50		

Table 3. Average charged multiplicities and dispersions in various angular regions for 100 GeV/c π^--nucleus interactions. Errors are statistical

Target	$0 < \theta_L < 3.5°$	$0 < \theta_L < 26°$	$26 < \theta_L < 110°$	$0 < \theta_L < 110°$	Dispersion $0 < \theta_L < 110°$
CH_2-C	3.32 ± 0.30	5.72 ± 0.30	0.83 ± 0.20	6.55 ± 0.20	2.9 ± 0.9
C	3.37 ± 0.10	6.19 ± 0.10	1.66 ± 0.10	7.85 ± 0.10	3.7 ± 0.1
Al	3.38 ± 0.20	6.24 ± 0.30	2.07 ± 0.10	8.31 ± 0.10	4.3 ± 0.2
Cu	3.30 ± 0.25	6.89 ± 0.30	2.83 ± 0.10	9.72 ± 0.10	4.8 ± 0.2
Ag	3.22 ± 0.30	7.23 ± 0.30	3.47 ± 0.20	10.7 ± 0.20	5.4 ± 0.3
Pb	3.23 ± 0.20	7.98 ± 0.30	4.20 ± 0.10	12.2 ± 0.20	5.8 ± 0.2
U	3.25 ± 0.30	7.48 ± 0.30	4.25 ± 0.20	11.7 ± 0.20	6.0 ± 0.3

Table 4. Average charged multiplicities and dispersions in various angular regions for 175 GeV/c π^- nucleus interactions. Errors are statistical.

Target	$0 \le \theta_L \le 26°$	$26° < \theta_L < 110°$	$0 \le \theta_L \le 110°$	Dispersion $0 < \theta_L < 110°$
CH_2-C	6.80 ± 0.20	1.02 ± 0.20	7.82 ± 0.30	3.5 ± 0.15
C	7.54 ± 0.23	1.78 ± 0.10	9.22 ± 0.10	4.5 ± 0.15
Cu	8.57 ± 0.30	2.82 ± 0.11	11.39 ± 0.20	5.6 ± 0.25
Pb	9.72 ± 0.32	4.55 ± 0.15	14.27 ± 0.15	7.0 ± 0.25

Table 5. Angular distributions and total multiplicities
for the various projectiles, momenta, and targets.
Upper values for each target refer to the mean
multiplicity in the indicated pseudorapidity range,
and lower values give the total error on that
multiplicity.

Pseudorapidity Range

	Tar-get	-0.67 / -0.38	-0.38 / 0.56	0.56 / 0.92	0.92 / 1.39	1.39 / 1.99	1.99 / 2.25	2.25 / 2.76	2.76 / 3.08	3.08 / 3.38	3.38 / 4.08	4.08 / 5.28	5.28 / 7.00	Mean Mult.
π^+A 50 GeV/c	H	0.0 / 0.06	0.13 / 0.12	0.17 / 0.08	0.41 / 0.12	0.91 / 0.18	0.51 / 0.12	1.08 / 0.22	0.68 / 0.15	0.61 / 0.12	1.22 / 0.22	0.66 / 0.41	0.33 / 0.01	6.70 / 0.63
	C	0.05 / 0.01	0.34 / 0.03	0.25 / 0.02	0.49 / 0.05	0.90 / 0.07	0.46 / 0.04	0.93 / 0.07	0.57 / 0.05	0.50 / 0.04	1.00 / 0.07	0.80 / 0.08	0.25 / 0.01	6.54 / 0.18
	Cu	0.26 / 0.05	1.17 / 0.08	0.59 / 0.05	0.90 / 0.08	1.40 / 0.11	0.66 / 0.06	1.23 / 0.10	0.72 / 0.07	0.59 / 0.05	1.11 / 0.08	0.78 / 0.17	0.34 / 0.04	9.76 / 0.30
	Pb	0.25 / 0.05	1.48 / 0.12	0.82 / 0.08	1.31 / 0.15	1.91 / 0.20	0.78 / 0.08	1.31 / 0.11	0.72 / 0.07	0.56 / 0.05	0.99 / 0.08	0.81 / 0.09	0.32 / 0.01	11.26 / 0.36
π^+A 100 GeV/c	H	0.09 / 0.04	0.33 / 0.08	0.20 / 0.08	0.38 / 0.13	0.72 / 0.15	0.40 / 0.08	0.85 / 0.12	0.50 / 0.10	0.55 / 0.10	1.19 / 0.17	1.56 / 0.20	0.73 / 0.09	7.58 / 0.42
	C	0.05 / 0.01	0.33 / 0.02	0.27 / 0.02	0.52 / 0.04	0.90 / 0.05	0.46 / 0.03	0.94 / 0.06	0.64 / 0.04	0.60 / 0.04	1.29 / 0.06	1.42 / 0.07	0.46 / 0.02	7.86 / 0.15
	Cu	0.13 / 0.04	0.76 / 0.07	0.47 / 0.05	0.82 / 0.09	1.35 / 0.11	0.65 / 0.06	1.25 / 0.09	0.79 / 0.07	0.72 / 0.06	1.47 / 0.09	1.24 / 0.10	0.64 / 0.02	10.29 / 0.26
	Pb	0.25 / 0.05	1.48 / 0.10	0.76 / 0.07	1.30 / 0.12	1.96 / 0.14	0.84 / 0.07	1.44 / 0.10	0.86 / 0.07	0.75 / 0.06	1.47 / 0.09	1.48 / 0.09	0.62 / 0.03	13.21 / 0.30
	U	0.29 / 0.06	1.62 / 0.13	0.85 / 0.09	1.46 / 0.16	2.17 / 0.19	0.91 / 0.09	1.56 / 0.12	0.93 / 0.08	0.81 / 0.07	1.59 / 0.11	1.76 / 0.13	0.63 / 0.04	14.57 / 0.39
π^+A 200 GeV/c	H	-0.03 / 0.15	-0.05 / 0.27	0.15 / 0.18	0.32 / 0.27	0.50 / 0.30	0.26 / 0.15	0.55 / 0.16	0.50 / 0.12	0.45 / 0.12	1.02 / 0.21	2.85 / 0.88	-0.03 / 0.41	6.49 / 1.17
	C	0.04 / 0.03	0.30 / 0.05	0.25 / 0.03	0.49 / 0.06	0.88 / 0.07	0.46 / 0.04	0.97 / 0.07	0.66 / 0.05	0.63 / 0.05	1.44 / 0.09	2.21 / 0.19	1.15 / 0.08	9.48 / 0.27
	Cu	0.11 / 0.04	0.77 / 0.18	0.50 / 0.10	0.89 / 0.14	1.46 / 0.18	0.70 / 0.10	1.38 / 0.16	0.88 / 0.12	0.81 / 0.11	1.84 / 0.19	2.99 / 0.62	1.27 / 0.13	13.61 / 0.77
	Ag	0.18 / 0.12	0.97 / 0.23	0.62 / 0.11	1.11 / 0.18	1.74 / 0.23	0.80 / 0.13	1.56 / 0.21	1.02 / 0.14	0.88 / 0.12	1.71 / 0.20	2.50 / 0.42	1.22 / 0.13	14.31 / 0.70
	Pb	0.25 / 0.09	1.46 / 0.19	0.82 / 0.13	1.40 / 0.21	2.12 / 0.25	0.90 / 0.12	1.53 / 0.17	1.03 / 0.12	0.95 / 0.11	1.85 / 0.17	2.69 / 0.29	1.17 / 0.13	16.17 / 0.61

	Tar-get	-0.67 -0.38	-0.38 0.56	0.56 0.92	0.92 1.39	1.39 1.99	1.99 2.25	2.25 2.76	2.76 3.08	3.08 3.38	3.38 4.08	4.08 5.28	5.28 7.00	Mean Mult.
pA 50 GeV/c	H	-0.06 0.12	0.0 0.24	0.17 0.15	0.56 0.15	1.23 0.19	0.46 0.11	0.56 0.15	0.36 0.10	0.44 0.09	1.02 0.16	0.64 0.16	0.29 0.03	5.69 0.51
	C	0.04 0.03	0.35 0.06	0.26 0.04	0.52 0.06	0.94 0.09	0.49 0.05	1.01 0.10	0.59 0.06	0.46 0.04	0.85 0.07	0.64 0.11	0.26 0.01	6.40 0.23
	Cu	0.14 0.06	0.93 0.12	0.57 0.08	0.98 0.12	1.55 0.15	0.69 0.08	1.26 0.13	0.71 0.08	0.56 0.05	0.97 0.09	0.60 0.28	0.31 0.07	9.27 0.43
	Pb	0.24 0.10	1.60 0.23	0.92 0.15	1.52 0.21	2.28 0.27	0.89 0.12	1.36 0.16	0.70 0.10	0.51 0.06	0.80 0.10	0.59 0.24	0.26 0.02	11.67 0.57
pA 100 GeV/c	H	-0.01 0.04	0.05 0.08	0.24 0.09	0.52 0.16	0.93 0.19	0.47 0.10	0.97 0.14	0.57 0.12	0.51 0.11	1.19 0.16	1.33 0.20	0.56 0.08	7.35 0.46
	C	0.05 0.01	0.34 0.03	0.28 0.03	0.55 0.05	0.98 0.06	0.50 0.04	1.04 0.06	0.67 0.05	0.59 0.04	1.17 0.06	1.06 0.06	0.49 0.02	7.72 0.16
	Cu	0.13 0.05	0.82 0.09	0.55 0.07	1.04 0.12	1.71 0.15	0.78 0.08	1.47 0.11	0.87 0.08	0.75 0.07	1.42 0.10	0.96 0.10	0.51 0.03	11.00 0.32
	Pb	0.27 0.05	1.65 0.12	0.93 0.09	1.65 0.17	2.52 0.20	1.05 0.10	1.76 0.12	1.00 0.09	0.83 0.07	1.44 0.10	1.09 0.09	0.56 0.03	14.75 0.38
	U	0.32 0.07	1.87 0.16	1.00 0.12	1.74 0.21	2.69 0.25	1.13 0.13	1.89 0.17	1.07 0.10	0.88 0.09	1.53 0.12	1.34 0.12	0.48 0.04	15.94 0.50
pA 200 GeV/c	H	-0.01 0.04	0.0 0.07	0.15 0.05	0.37 0.10	0.71 0.12	0.37 0.07	0.81 0.12	0.56 0.09	0.54 0.08	1.23 0.14	1.57 0.22	0.98 0.10	7.29 0.30
	C	0.04 0.01	0.32 0.03	0.27 0.02	0.53 0.04	0.96 0.05	0.51 0.03	1.08 0.06	0.72 0.04	0.67 0.04	1.50 0.07	1.82 0.11	0.30 0.03	9.34 0.18
	Cu	0.14 0.03	0.87 0.08	0.58 0.05	1.06 0.09	1.76 0.12	0.84 0.07	1.64 0.11	1.05 0.08	0.94 0.07	1.99 0.11	2.21 0.20	0.94 0.04	14.01 0.34
	Ag	0.19 0.04	1.07 0.09	0.68 0.06	1.25 0.11	2.02 0.14	0.93 0.08	1.74 0.12	1.09 0.08	0.98 0.07	1.99 0.11	2.04 0.16	0.97 0.05	14.95 0.34
	Pb	0.28 0.05	1.69 0.12	0.97 0.08	1.74 0.15	2.71 0.19	1.18 0.09	2.09 0.14	1.25 0.09	1.09 0.08	2.16 0.12	2.23 0.15	1.08 0.05	18.47 0.40

Pseudorapidity Range

Pseudorapidity Range

	Target	-0.67 -0.38	-0.38 0.56	0.56 0.92	0.92 1.39	1.39 1.99	1.99 2.25	2.25 2.76	2.76 3.08	3.08 3.38	3.38 4.08	4.08 5.28	5.28 7.00	Mean Mult.
K+ 50 GeV/c	C	0.02 0.06	0.24 0.14	0.23 0.09	0.52 0.13	0.90 0.18	0.43 0.11	0.89 0.20	0.56 0.13	0.50 0.10	1.00 0.18	0.72 0.28	0.31 0.01	6.31 0.52
	Cu	0.10 0.09	0.83 0.26	0.51 0.21	0.86 0.70	1.26 0.86	0.57 0.19	1.12 0.25	0.69 0.17	0.61 0.14	1.23 0.24	1.02 0.74	0.46 0.03	9.26 1.45
	Pb	0.23 0.22	1.53 0.52	0.85 0.34	1.33 0.43	1.80 0.54	0.71 0.26	1.24 0.39	0.70 0.26	0.56 0.16	1.02 0.28	0.94 0.56	0.42 0.15	11.35 1.29
K+ 100 GeV/c	C	0.04 0.03	0.30 0.05	0.20 0.03	0.37 0.05	0.69 0.07	0.39 0.05	0.82 0.09	0.53 0.06	0.47 0.05	1.07 0.09	1.64 0.26	0.41 0.07	6.92 0.33
	Cu	0.08 0.13	0.60 0.23	0.36 0.14	0.61 0.18	1.16 0.25	0.60 0.15	1.12 0.26	0.68 0.17	0.61 0.14	1.24 0.25	1.12 0.91	0.71 0.04	8.89 1.10
	Pb	0.27 0.10	1.64 0.21	0.83 0.14	1.16 0.17	1.64 0.22	0.75 0.12	1.39 0.19	0.84 0.13	0.73 0.10	1.51 0.17	1.77 0.59	0.39 0.14	12.92 0.79
	U	0.24 0.15	1.58 0.36	0.86 0.23	1.34 0.30	1.93 0.37	0.82 0.19	1.48 0.29	0.88 0.19	0.76 0.15	1.49 0.26	1.16 1.03	0.38 0.18	12.93 1.33

Pseudorapidity Range

$\bar{P}A$ 200 GeV/c

Tar-get	-0.67 / -0.38	-0.38 / 0.56	0.56 / 0.92	0.92 / 1.39	1.39 / 1.99	1.99 / 2.25	2.25 / 2.76	2.76 / 3.08	3.08 / 3.38	3.38 / 4.08	4.08 / 5.28	5.28 / 7.00	Mean Mult.
C	0.14 / 0.08	0.55 / 0.12	0.28 / 0.07	0.42 / 0.11	0.77 / 0.14	0.45 / 0.10	0.98 / 0.19	0.66 / 0.12	0.63 / 0.12	1.43 / 0.22	1.69 / 0.71	1.20 / 0.22	9.19 / 0.85
Cu	0.09 / 0.34	0.82 / 0.80	0.60 / 0.51	1.22 / 0.60	2.09 / 0.87	0.91 / 0.51	1.75 / 0.87	1.08 / 0.59	0.92 / 0.46	1.79 / 0.81	1.27 / 0.79	0.94 / 0.08	13.49 / 2.23
Ag	0.29 / 0.27	1.50 / 0.64	0.87 / 0.42	1.47 / 0.58	2.59 / 0.86	1.22 / 0.50	2.16 / 0.81	1.26 / 0.54	1.06 / 0.42	2.10 / 0.76	2.27 / 0.82	1.16 / 0.36	17.96 / 2.12
Pb	0.42 / 0.27	1.78 / 0.66	1.04 / 0.44	1.82 / 0.61	3.00 / 0.84	1.29 / 0.45	2.13 / 0.72	1.14 / 0.47	0.92 / 0.30	1.40 / 0.53	-0.88 / 2.19	1.97 / 0.38	16.04 / 2.83

π⁻A 200 GeV/c

Target	Pseudorapidity Range												Mean Mult.
	-0.67 / -0.38	-0.38 / 0.56	0.56 / 0.92	0.92 / 1.39	1.39 / 1.99	1.99 / 2.25	2.25 / 2.76	2.76 / 3.08	3.08 / 3.38	3.38 / 4.08	4.08 / 5.28	5.28 / 7.00	
H	0.01 / 0.04	0.10 / 0.07	0.12 / 0.04	0.30 / 0.07	0.66 / 0.10	0.36 / 0.06	0.71 / 0.12	0.48 / 0.05	0.44 / 0.08	1.11 / 0.15	2.43 / 0.60	1.10 / 0.13	7.81 / 0.67
C	0.04 / 0.01	0.29 / 0.02	0.22 / 0.02	0.44 / 0.04	0.83 / 0.06	0.45 / 0.04	0.94 / 0.07	0.64 / 0.05	0.61 / 0.05	1.43 / 0.09	2.03 / 0.24	1.07 / 0.04	8.99 / 0.29
Cu	0.11 / 0.04	0.76 / 0.08	0.47 / 0.05	0.83 / 0.09	1.39 / 0.13	0.69 / 0.07	1.36 / 0.12	0.88 / 0.08	0.82 / 0.08	1.84 / 0.15	2.38 / 0.41	1.08 / 0.07	12.60 / 0.52
Ag	0.15 / 0.03	0.98 / 0.08	0.58 / 0.05	0.98 / 0.10	1.59 / 0.14	0.76 / 0.08	1.45 / 0.13	0.91 / 0.08	0.82 / 0.07	1.80 / 0.13	2.69 / 0.37	1.14 / 0.04	13.86 / 0.48
Pb	0.23 / 0.04	1.41 / 0.10	0.83 / 0.07	1.40 / 0.13	2.20 / 0.18	0.97 / 0.09	1.70 / 0.13	1.03 / 0.09	0.92 / 0.07	1.95 / 0.13	2.49 / 0.35	1.20 / 0.06	16.31 / 0.49

Table 6

Coefficients determined from the parameterization of the angular distributions as $N(\Delta\eta) = a + b\bar{\nu} + c\bar{\nu}^2 + d\bar{\nu}^3$. The order of the polynomial used was governed by the precision of fit. Fractional errors at integer values of $\bar{\nu}$ are indicated by $\sigma_1, \sigma_2,$ and σ_3 for $\bar{\nu} = 1$, 2, and 3 respectively. The entry "x" signifies a fractional error greater than 1.0.

50 GeV π^+A							
$\Delta\eta$		a	b	c	σ_1	σ_2	σ_3
-0.67	-0.38	-0.19	0.19		x	.16	.18
-0.38	0.56	-0.57	0.65	0.06	.36	.07	.09
0.56	0.92	-0.16	0.29	0.03	.25	.09	.12
0.92	1.39	-0.11	0.46	0.02	.14	.09	.11
1.39	1.99	0.09	0.65		.09	.08	.09
1.99	2.25	0.19	0.22		.12	.08	.09
2.25	2.76	0.62	0.27		.09	.08	.09
2.76	3.08	0.47	0.10		.09	.09	.10
3.08	3.38	0.47	0.04		.08	.08	.08
3.38	4.08	1.11	-0.04		.07	.07	.07
4.08	5.28	0.78			.12	.12	.12
5.28	7.00	0.31			.03	.03	.03

100 GeV π^+A							
$\Delta\eta$		a	b	c	σ_1	σ_2	σ_3
-0.67	-0.38	0.01	-0.02	0.04	.75	.23	.19
-0.38	0.56	0.02	-0.02	0.20	.20	.09	.07
0.56	0.92	-0.04	0.20	0.03	.16	.08	.09
0.92	1.39	-0.16	0.53		.14	.08	.10
1.39	1.99	0.01	0.70		.08	.06	.07
1.99	2.25	0.15	0.25		.10	.08	.09
2.25	2.76	0.60	0.24	0.03	.08	.07	.07
2.76	3.08	0.24	0.34	-0.03	.09	.08	.09
3.08	3.38	0.34	0.24	-0.03	.07	.07	.08
3.38	4.08	1.00	0.27	-0.02	.06	.06	.06
4.08	5.28	1.47	0.02		.05	.05	.06
5.28	7.00	0.35	0.11		.04	.04	.04

200 GeV π^+A							
$\Delta\eta$		a	b	c	σ_1	σ_2	σ_3
-0.67	-0.38	-0.07	0.07	0.01	x	.25	.27
-0.38	0.56	-0.24	0.28	0.11	.47	.11	.12
0.56	0.92	-0.11	0.26	0.02	.29	.10	.14
0.92	1.39	-0.32	0.60		.25	.10	.14
1.39	1.99	-0.39	1.06	-0.06	.15	.07	.11
1.99	2.25	0.04	0.32		.14	.09	.11
2.25	2.76	0.27	0.51		.10	.07	.09
2.76	3.08	0.27	0.29		.11	.08	.10
3.08	3.38	0.27	0.28		.11	.07	.10
3.38	4.08	0.66	0.74	-0.10	.07	.06	.08
4.08	5.28	1.58	0.52		.09	.07	.07
5.28	7.00	1.17			.05	.05	.05

200 GeV π^-A							
$\Delta\eta$		a	b	c	σ_1	σ_2	σ_3
-0.67	-0.38	0.01	-0.03	0.03	x	.30	.20
-0.39	0.56	-0.13	0.13	0.14	.29	.09	.07
0.56	0.92	-0.02	0.09	0.07	.21	.09	.09
0.92	1.39	0.08	0.12	0.11	.16	.09	.10
1.39	1.99	0.29	0.20	0.16	.11	.08	.08
1.99	2.25	0.17	0.16	0.04	.11	.09	.09
2.25	2.76	0.31	0.48		.09	.07	.07
2.76	3.08	0.28	0.25		.08	.07	.08
3.08	3.38	0.12	0.44	-0.06	.10	.08	.08
3.38	4.08	0.31	1.06	-0.17	.08	.06	.07
4.08	5.28	1.66	0.37		.13	.11	.11
5.28	7.00	0.97	0.07		.05	.04	.06

50 GeV K$^+$A						
$\Delta\eta$		a	b	c	σ_1	σ_2	σ_3
-0.67	-0.38	-0.18	0.16		x	.71	.83
-0.38	0.56	-1.06	1.05		x	.22	.25
0.56	0.92	-0.40	0.51		x	.23	.30
0.92	1.39	-0.32	0.68		.47	.25	.33
1.39	1.99	-0.03	0.75		.32	.21	.32
1.99	2.25	0.15	0.23		.37	.21	.35
2.25	2.76	0.48	0.33		.31	.18	.33
2.76	3.08	0.41	0.13		.30	.19	.39
3.08	3.38	0.46	0.05		.16	.14	.17
3.38	4.08	1.14	0.04		.12	.12	.12
4.08	5.28	0.87			.26	.26	.26
5.28	7.00	0.31			.03	.03	.03

100 GeV K$^+$A						
$\Delta\eta$		a	b	c	σ_1	σ_2	σ_3
-0.67	-0.38	-0.17	0.17		x	.35	.36
-0.38	0.56	-0.32	0.23	0.21	.67	.11	.17
0.56	0.92	-0.12	0.14	0.09	.45	.13	.23
0.92	1.39	-0.18	0.32	0.09	.26	.12	.16
1.39	1.99	-0.32	0.81		.16	.10	.12
1.99	2.25	-0.01	0.32		.16	.11	.14
2.25	2.76	0.21	0.49		.14	.10	.13
2.76	3.06	0.16	0.27		.13	.11	.14
3.08	3.38	0.20	0.22		.14	.06	.13
3.38	4.08	0.61	0.35		.10	.09	.12
4.08	5.28	1.43			.15	.15	.15
5.28	7.00	0.64			.06	.06	.06

50 GeV pA						
$\Delta\eta$		a	b	c	σ_1	σ_2	σ_3
-0.67	-0.38	-0.09	0.09		x	.30	.33
-0.38	0.56	-0.31	0.37	0.06	.92	.12	.10
0.56	0.92	-0.09	0.22	0.02	.47	.14	.12
0.92	1.39	-0.01	0.37	0.02	.21	.10	.11
1.39	1.99	0.23	0.52	0.02	.12	.08	.09
1.99	2.25	0.16	0.22		.15	.10	.10
2.25	2.76	0.26	0.60	-0.08	.14	.09	.09
2.76	3.08	0.25	0.28	-0.04	.14	.09	.11
3.08	3.38	0.38	0.08	-0.01	.09	.08	.08
3.38	4.08	1.00	-0.08	0.01	.08	.08	.07
4.08	5.28	0.65			.14	.14	.14
5.28	7.00	0.26			.04	.04	.04

100 GeV pA						
$\Delta\eta$		a	b	c	σ_1	σ_2	σ_3
-0.67	-0.38	-0.11	0.11		x	.18	.18
-0.38	0.56	-0.47	0.53	0.02	.38	.07	.07
0.56	0.92	-0.14	0.31		.13	.07	.08
0.92	1.39	-0.13	0.50		.11	.07	.08
1.39	1.99	0.07	0.63	0.02	.08	.06	.06
1.99	2.25	0.13	0.27		.10	.06	.07
2.25	2.76	0.41	0.49	-0.02	.07	.05	.06
2.76	3.08	0.32	0.30	-0.03	.07	.06	.06
3.08	3.38	0.28	0.27	-0.03	.08	.06	.06
3.38	4.08	0.70	0.44	-0.06	.06	.05	.05
4.08	5.28	1.10	0.04		.06	.06	.06
5.28	7.00	0.50			.04	.04	.04

200 GeV pA								
$\Delta\eta$		a	b	c	d	σ_1	σ_2	σ_3
-0.67	-0.38	-0.11	0.11			x	.20	.19
-0.38	0.56	-1.34	1.90	-0.68	0.11	x	.08	.07
0.56	0.92	-0.34	0.62	-0.18	0.03	.15	.07	.07
0.92	1.39	-0.27	0.71	-0.15	0.03	.16	.08	.07
1.39	1.99	0.02	0.58	0.05		.09	.06	.06
1.99	2.25	0.07	0.30			.08	.06	.07
2.25	2.76	0.26	0.59	-0.02		.07	.06	.05
2.76	3.08	0.18	0.43	-0.04		.07	.06	.06
3.08	3.38	0.08	0.51	-0.07		.10	.06	.06
3.38	4.08	0.21	1.14	-0.16		.07	.04	.05
4.08	5.28	1.26	0.51	-0.07		.07	.06	.06
5.28	7.00	0.80	0.07			.05	.03	.04

200 GeV $\bar{p}$A							
$\Delta\eta$		a	b	c	σ_1	σ_2	σ_3
-0.67	-0.38	-0.04	0.11		x	.39	.48
-0.38	0.56	-0.39	0.59		.95	.16	.21
0.56	0.92	-0.31	0.39		x	.18	.24
0.92	1.39	-0.59	0.64		x	.17	.22
1.39	1.99	-0.79	0.98		x	.14	.18
1.99	2.25	-0.10	0.35		.60	.17	.22
2.25	2.76	0.31	0.46		.44	.19	.22
2.76	3.08	0.35	0.22		.40	.21	.26
3.08	3.38	0.40	0.15		.27	.16	.18
3.38	4.08	1.26	0.12		.19	.13	.15
4.08	5.28	2.24			.13	.13	.15
5.28	7.00	1.01			.08	.08	.09

Table 7. Parameterization of $\bar{\nu}$ as a function of atomic number A for incident hadrons (π, K, or p). The magnitude of the resulting fractional error $d\bar{\nu}/\bar{\nu}$ is also shown (the lower value refers to Be nucleus, the upper value to U).

Incident Momentum (GeV/c)	Projectile	$\bar{\nu}$
50	π^+	$0.648 \ A^{0.271}$
	K^+	$0.686 \ A^{0.235}$
	P	$0.653 \ A^{0.310}$
100	π^+	$0.645 \ A^{0.274}$
	π^-	$0.672 \ A^{0.273}$
	K^+	$0.677 \ A^{0.242}$
	P	$0.656 \ A^{0.313}$
175	π^-	$0.677 \ A^{0.273}$
200	π^+	$0.645 \ A^{0.276}$
	π^-	$0.674 \ A^{0.274}$
	P	$0.657 \ A^{0.316}$
	$\bar{P}$	$0.744 \ A^{0.306}$
$d\bar{\nu}/\bar{\nu}$	π^+	$0.014 \to 0.032$
	π^-	$0.014 \to 0.015$
	K^+	$0.019 \to 0.037$
	P	$0.009 \to 0.014$
	$\bar{P}$	$0.020 \to 0.026$

Table 8. Comparison of π^-A total charged multiplicities $\langle n\rangle_1^C$ from Part I and $\langle n\rangle_2$ from Part II where $\langle n\rangle_1^C$ = $C_A C_R C_H \langle n\rangle_1$ at 100 GeV/c, and $C_A C_N C_H \langle n\rangle_1$ at 175 GeV/c. The C's are multiplicative factors required to compare the two sets of data. $\langle n\rangle_1$'s are measured multiplicities from Part I.

Incident Beam Momentum (GeV/c)	Target	$\langle n\rangle_1$	Acceptance Factor C_A	Incident Particle Factor C_R	Hodoscope Factor C_H	$\langle n\rangle_1^C$	$\langle n\rangle_2$
100	C	7.9	1.01	1.04	1.01	8.4 ± 0.1	7.9 ± 0.2
100	Cu	9.7	1.01	1.04	1.02	10.4 ± 0.1	10.3 ± 0.3
100	Pb	12.2	1.02	1.01	1.05	13.2 ± 0.2	13.2 ± 0.3
100	U	11.7	1.02	1.01	1.05	12.6 ± 0.2	14.6 ± 0.4

Incident Beam Momentum (GeV/c)	Target	$\langle n\rangle_1$	Acceptance Factor C_A	Beam Momentum Factor C_N	Hodoscope Factor C_H	$\langle n\rangle_1^C$	$\langle n\rangle_2$
175	C	9.2	1.00	1.03	1.01	9.6 ± 0.1	9.0 ± 0.3
175	Cu	11.4	1.01	1.03	1.04	12.1 ± 0.2	12.6 ± 0.5
175	Pb	14.3	1.01	1.03	1.07	15.8 ± 0.2	16.3 ± 0.6

Table 9. Comparison of π^-p charged multiplicities and dispersions. Bubble chamber data are from Ref. 10 (100 GeV/c), Ref. 11 (147 GeV/c), and Ref. 12 (205 GeV/c).

Incident Momentum (GeV/c)	Multiplicity		Dispersion	
	This Experiment	Bubble Chamber	This Experiment	Bubble Chamber
100	6.55 ± 0.20	6.79 ± 0.08	2.90 ± 0.10	3.16 ± 0.04
147	----	7.34 ± 0.10	----	3.58 ± 0.05
175	7.82 ± 0.30	----	3.50 ± 0.15	----
205	----	8.02 ± 0.12	----	3.91 ± 0.11

Table 10. Average charged multiplicities for hadron-proton interactions. Multiplicities are obtained from using the parameterization described in Section V. Comparison is made with fitted bubble chamber results from Ref. 13.

Incident Beam Momentum (GeV/c)	Projectile Type	This Experiment $\langle n \rangle_{CH_2-C}$	Fitted Value -0.5 $\langle n \rangle_{hp}$
50	p	5.37 ± 0.26	4.78
100	p	6.42 ± 0.16	5.94
200	p	7.12 ± 0.20	7.24
50	K^+	5.68 ± 0.57	5.25
100	K^+	5.87 ± 0.31	6.41
50	π^+	5.94 ± 0.19	5.40
100	π^+	7.04 ± 0.18	6.47
200	π^+	8.05 ± 0.29	7.67
200	π^-	7.71 ± 0.32	7.49
200	$\bar{p}$	7.34 ± 0.72	7.55

Table 11. Average charged multiplicities of relativistic ($\beta \gtrsim 0.85$ this experiment, $\beta \gtrsim 0.7$ other data) secondaries in hadron-emulsion interactions. Results from this experiment are obtained from the parameterization described in Section V. $\bar{\nu}$ values of 2.32, 2.39, 1.96, and 2.06 were used in 50 GeV p-Em, 200 GeV p-Em, 50 GeV π^+-Em, and 200 GeV π^--Em respectively.

Incident Beam Momentum (GeV/c)	Projectile Type	This Experiment	Other Data	
50	p	8.91 ± 0.27	8.7 ± 0.1	(Ref. 18)
200	p	13.36 ± 0.25	13.2 ± 0.2 13.4 ± 0.2 13.8 ± 0.2	(Ref. 19) (Ref. 16) (Ref. 18)
50	π^+	9.05 ± 0.23		
60	π^+		8.6 ± 0.2	(Ref. 20)
200	π^-	12.46 ± 0.37	11.4 ± 0.1 12.0 ± 0.2	(Ref. 16) (Ref. 6)

Table 12. Results of fitting scaled multiplicity as a function
           of nuclear thickness assuming: (a) A linear relation-
           ship, $R_A = a + b\bar{\nu}$; (b) A power law relationship, $R_A =$
           $R_1 A^\alpha$. Errors on the fit parameters are highly corre-
           lated. $P(\chi^2)$ is the probability of getting a χ^2 great-
           er than the observed value. Probabilities less than
           0.5% are signified by ---.

Table 12 (a)

Incident beam Momentum (GeV/c)	Projectile Type	a	b	$P(\chi^2)$
50	π^+	0.41 ± 0.08	0.64 ± 0.05	.02
50	K^+	0.17 ± 0.33	0.84 ± 0.22	.81
50	p	0.55 ± 0.12	0.57 ± 0.06	.52
50	π^+, K^+, p	0.45 ± 0.06	0.62 ± 0.04	.32
100	π^+	0.46 ± 0.05	0.58 ± 0.03	.08
100	K^+	0.16 ± 0.14	0.74 ± 0.09	.67
100	p	0.45 ± 0.06	0.59 ± 0.03	.50
100	π^+, K^+, p	0.43 ± 0.03	0.60 ± 0.02	.27
200	π^+	0.50 ± 0.10	0.58 ± 0.05	.64
200	π^-	0.39 ± 0.09	0.61 ± 0.05	.90
200	p	0.45 ± 0.05	0.58 ± 0.02	.14
200	$\bar{p}$	0.35 ± 0.28	0.55 ± 0.13	.35
200	π^+, π^-, p, $\bar{p}$	0.45 ± 0.04	0.58 ± 0.02	.53
50 100 200	π^+, π^-, K^+, p, $\bar{p}$	0.45 ± 0.02	0.59 ± 0.01	.25

Table 12 (b)

Incident beam Momentum (GeV/c)	Projectile Type	R_1	α	$P(\chi^2)$
50	π	0.75 ± 0.04	0.20 ± 0.01	.04
50	K^+	0.71 ± 0.10	0.21 ± 0.04	.82
50	p	0.79 ± 0.06	0.21 ± 0.02	.73
50	π^+, K^+, p	0.76 ± 0.03	0.21 ± 0.01	.01
100	π^+	0.74 ± 0.03	0.19 ± 0.01	.03
100	K^+	0.63 ± 0.06	0.22 ± 0.02	.66
100	p	0.72 ± 0.03	0.23 ± 0.01	.25
100	π^+, K^+, p	0.71 ± 0.02	0.22 ± 0.01	----
200	π^+	0.78 ± 0.05	0.19 ± 0.02	.76
200	π^-	0.72 ± 0.05	0.21 ± 0.02	.80
200	p	0.72 ± 0.03	0.23 ± 0.01	.11
200	$\bar{p}$	0.67 ± 0.14	0.25 ± 0.05	.39
200	π^+, π^-, p, $\bar{p}$	0.75 ± 0.02	0.21 ± 0.01	----
200	π^+, π^-, K^+ p, $\bar{p}$	0.73 ± 0.01	0.21 ± 0.004	---

FIGURE CAPTIONS

1. Details of the apparatus. The scale refers only to the region between counters V2 and W2.

2. Cerenkov light output from UVT lucite as a function of velocity (or momentum).

3. Typical pulse height spectrum obtained with the "C" counter. Pulse height is measured in arbitrary units.

4.a Location of experiment in M6 beam line. The scale refers only to the region between counters VO and C.

4.b Details of the apparatus.

5. Acceptance of the apparatus. H refers to the wide-angle hodoscope, R1, R2, and R3 to the three lucite-scintillator ring hodoscopes, and C to the Cerenkov counter.

6. Probability $P(\nu)$ of an incident hadron (K^+ or p) having ν collisions within a nucleus (carbon or uranium).

7. Comparison of 100 GeV/c π^+p, K^+p, and pp laboratory rapidity distributions. Data are from this experiment (histogram) and Ref. 15 (points). The pseudorapidity variable (η) refers to this experiment, the rapidity variable (y) to Ref. 15. Reference data have been renormalized by subtracting 0.5 particles from their published multiplicities. No attempt has been made to normalize the two sets of data with respect to one another.

8. Comparison of 100 GeV/c pp pseudorapidity distributions. Data are from this experiment (histogram) and Ref. 8 (points). Both sets of data have been subjected to a velocity cut ($\beta > 0.85$), an angular acceptance cut (events with any track having $\eta > 7$ omitted), and a multiplicity cut (total multiplicity ≤ 2 rejected). Errors have been omitted in the interest of clarity. No overall normalization has been attempted between the two sets of data.

9. Comparison of (a) 200 GeV p-emulsion and (b) π^--emulsion pseudorapidity distributions. Interpolated results from this experiment (solid histogram) are compared with data from Ref. 17 (dashed histogram) and Ref. 16 (points). No relative

normalization has been attempted.

10. Exponent α where the inclusive cross section $\sigma(\Delta\eta)/\Delta\eta$ is assumed to follow the form $A^{\alpha(\eta)}$. The from $A^{0.69}$ has been assumed for the total inelastic cross section so that data from this experiment (histogram) can be compared directly with data from Ref. 21. (Points refer to positively charged secondaries, crosses refer to negatives).

11. Comparison of pseudorapidity distributions for $\eta \gtrsim 1.5$ for 200 GeV pA interactions from this experiment (histogram) and nA interactions from Ref. 22 (points).

12. Scaled multiplicity $R_A = \langle n \rangle_{hA}/\langle n \rangle_{hp}$ vs. nuclear thickness as measured in terms of $\bar{\nu}$.

13. Scaled multiplicity $R_A = \langle n \rangle_{hA}/\langle n \rangle_{hp}$ vs. nuclear thickness as measured in terms of $\bar{\nu}'$.

14. Scaled multiplicity as a function of nuclear thickness. The solid line is a result of the fit $R_A = a + b\bar{\nu}$, the dashed line, $R_A = 1 - b + b\bar{\nu}$. Data are for incident momenta (a) 50 GeV/c, (b) 100 GeV/c, (c) 200 GeV/c. Only multiplicities from Part II (Table 5) are included in the fit. Effects of errors on $\bar{\nu}$ are included in the fitting procedure.

15. Scaled multiplicity from proton-included interactions as a function of energy for 3 nuclear targets, C, Cu, and Pb. Hadron-nucleus multiplicities are from Table 10.

16. Dispersion vs. mean of multiplicity distribution for $\pi^- A$ interactions at 100 and 175 GeV/c. Data are from Tables 3 and 4. For comparison, the best fit to $\pi^- p$ data from Ref. 25 is also shown.

17. Exponent α' where the normalized inclusive cross section $1/\sigma_{Tot}$ $\sigma(\Delta\eta)/\Delta\eta$ is assumed to follow the form $A^{\alpha'(\eta)}$. p, π^+, π^-, K^+ and $\bar{p}$-induced data are shown in (a), (b), (c), (d), and (e) respectively. p-induced data are superimposed on $\bar{p}$ data for comparison.

18. Angular distributions of charged secondaries at 3 incident momenta for various nuclear thicknesses. Data are for (a) incident p, (b) incident π^+ at 50, 100 and 200 GeV/c. The distributions for $\bar{\nu}$ = 2,3 and 4 have been offset by 2,5 and 8

units in order to provide separation of the results.

19. Angular distributions of charged secondaries as measured in the rest frame of the incident projectile for incident 50, 100 and 200 GeV/c momenta. $\eta' = \eta + \S$, where $\S$ is the rapidity boost. Data are from (a) lead, (b) copper, and (c) carbon targets. Hadron-nucleon data from this experiment are also shown, as a solid curve. Error bars are omitted for reasons of clarity.

20. Projectile and target fragmentation regions for incident protons, K^+'s and π^+'s. The angluar distributions are measured in the laboratory frame for the target fragmentation region and rest frame of the incident projectile for the projectile fragmentation region. The dashed curve shows corresponding hydrogen data for incident pions and protons. The corresponding curve for incident kaons was unobtainable due to lack of statistical accuracy.

21. (a) Angular distribution from π^+-induced interactions normalized to proton-induced interactions. Laboratory distributions have been boosted to the rest frame of an incident proton. Data are from a lead target. (b) Similar to (a), except distributions normalized to hydrogen were used. Data are for $\bar{\nu} = 3$.

22. Nuclear thickness variation of pseudorapidity distributions of charged secondaries. Data are for incident
    (a) 50 GeV/c π^+'s   (b) 100 GeV/c π^+'s,
    (c) 200 GeV/c π^+'s,   (d) 200 GeV/c π^-'s,
    (e) 50 GeV/c K^+'s,   (f) 100 GeV/c K^+'s,
    (g) 50 GeV/c p's,   (h) 100 GeV/c p's,
    (i) 200 GeV/c p's

23. Multiplicities in the central region. Only high statistics data were used. The central region is defined as 2.76 $<\eta<$ 1.99 for 50 GeV/c data, 3.08 $<\eta<$ 2.25 for 100 GeV/c, and 3.88 $<\eta<$ 2.76 for 200 GeV/c. Error envelopes of experimental data are shown. Left-hand scale is appropriate for solid envelopes, right-hand scale for dashed ones.
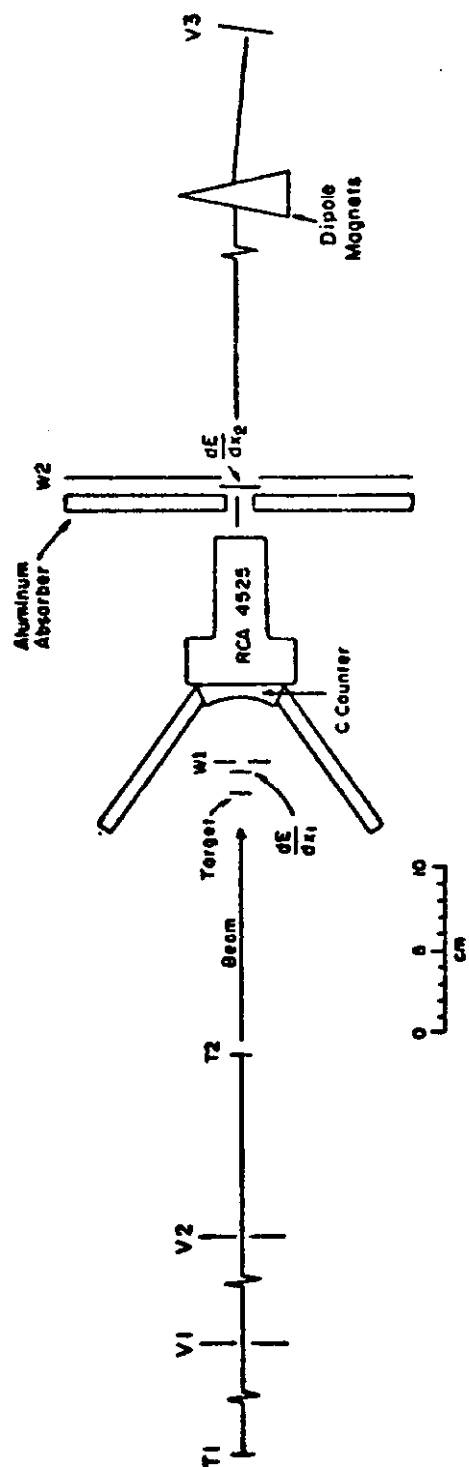
Fig. 1.

Fig. 2.

Fig. 3.

Fig. 4 (a).

Fig. 4 (b).

PART I

PART II

C

C

H

C

R1 R2 R3

H

C

R1

R2 R3

H

R1 R3

R2

C

H

θ_L
(DEGREES)   130   90   50   20 10   5   2   1   0.5

η 0   2   4   6

$\left[= - \ln \left(\tan \left(\theta / 2 \right) \right) \right]$
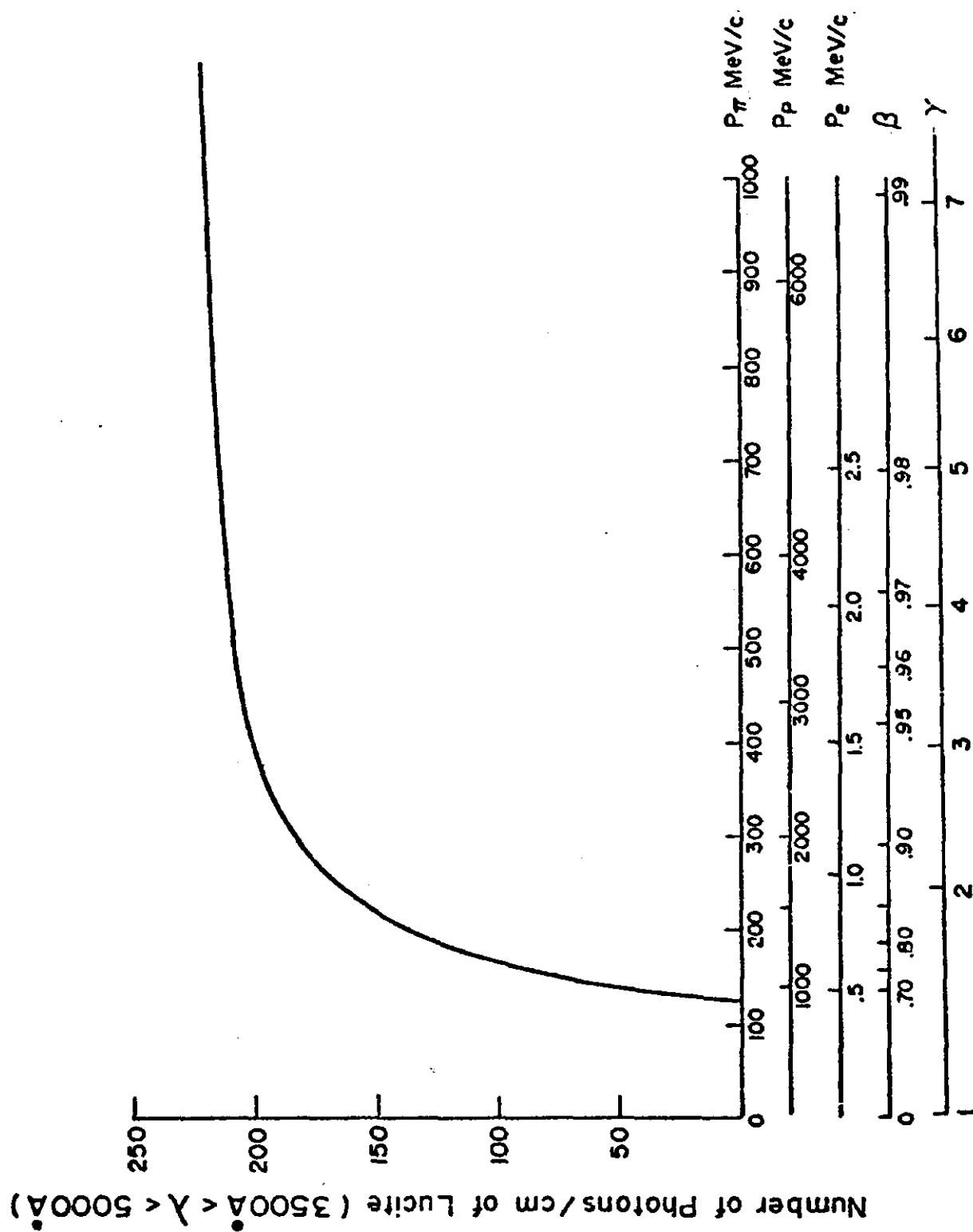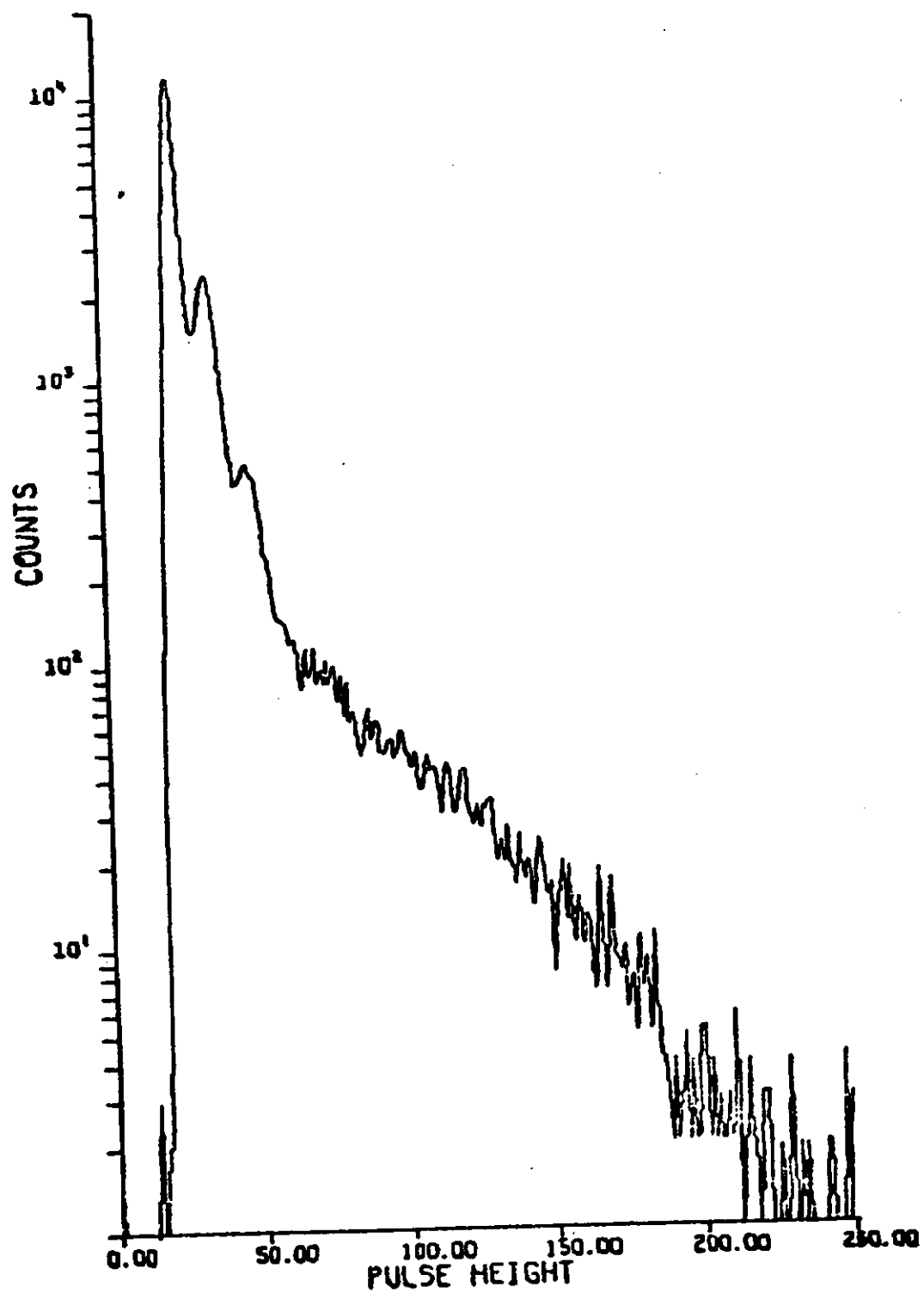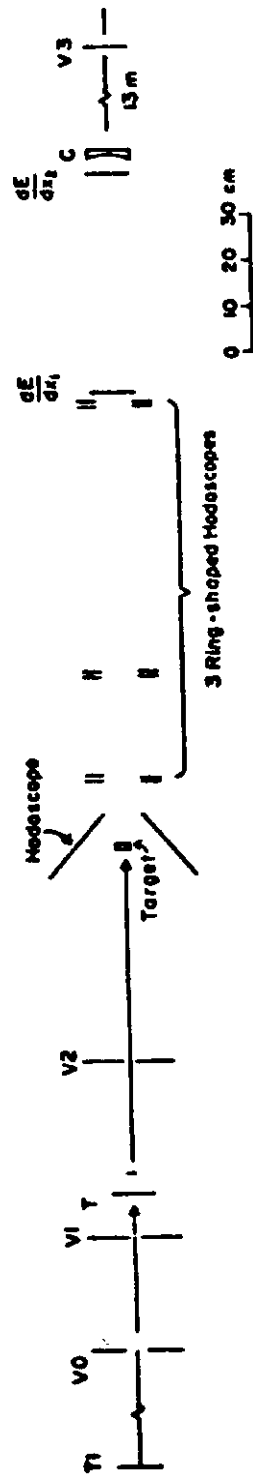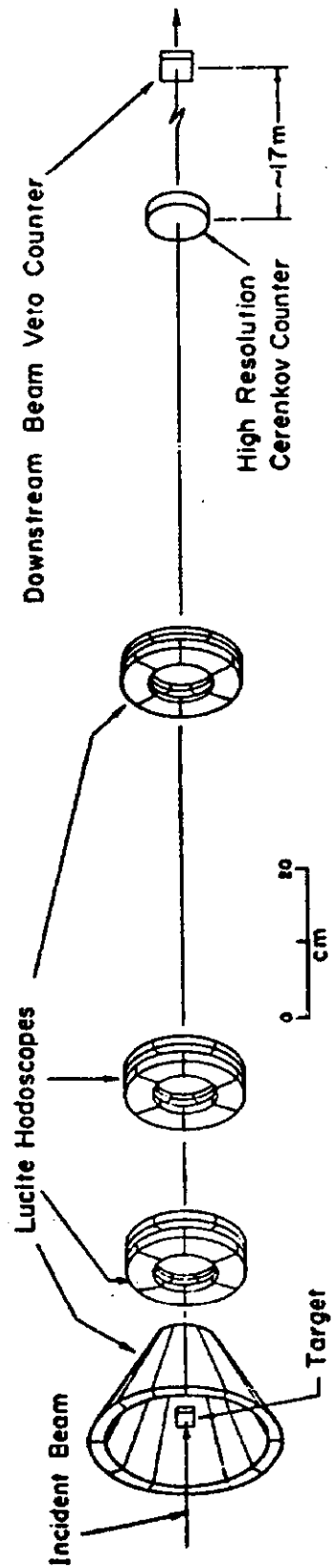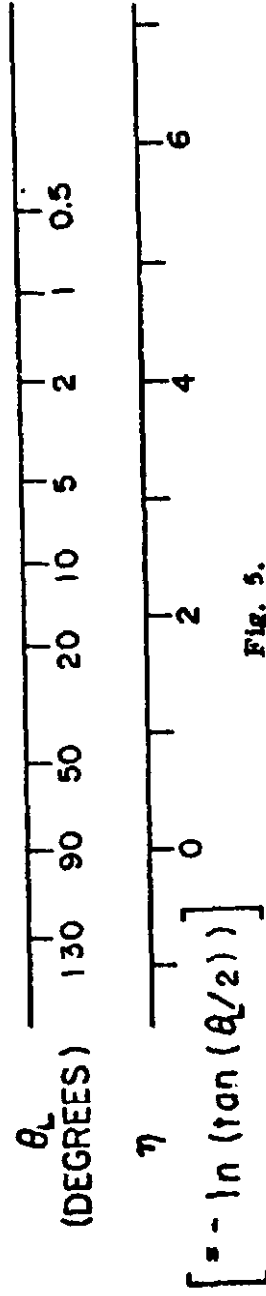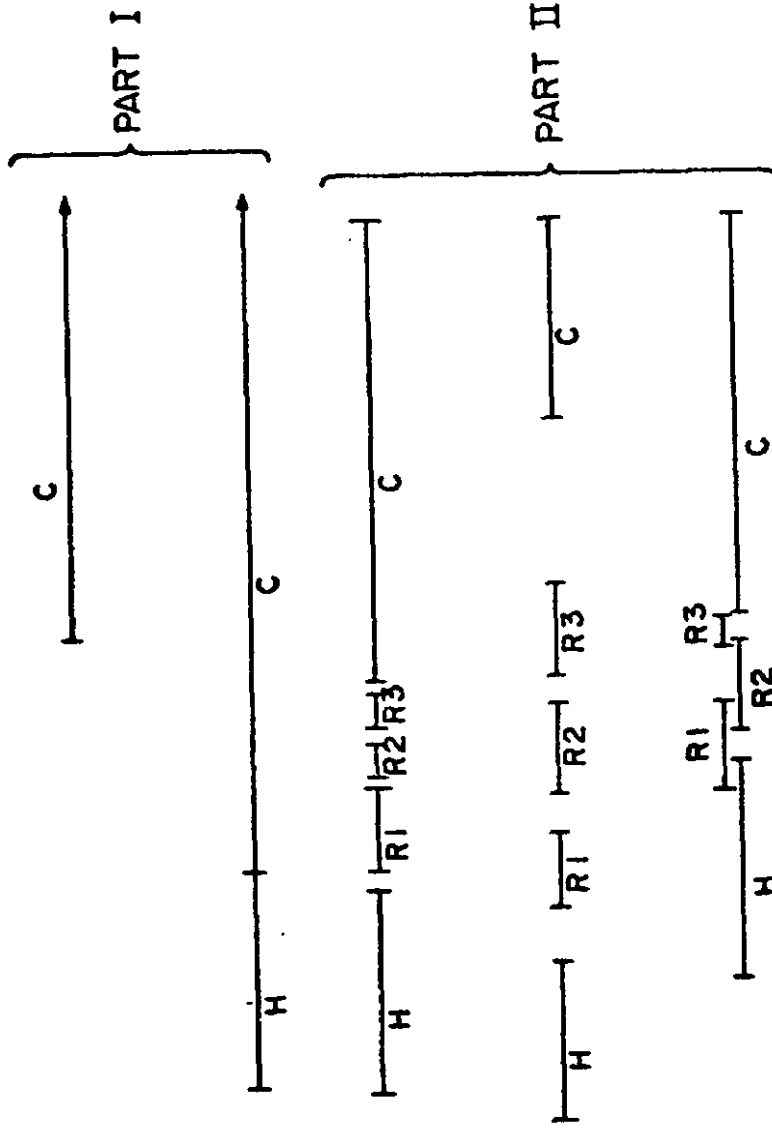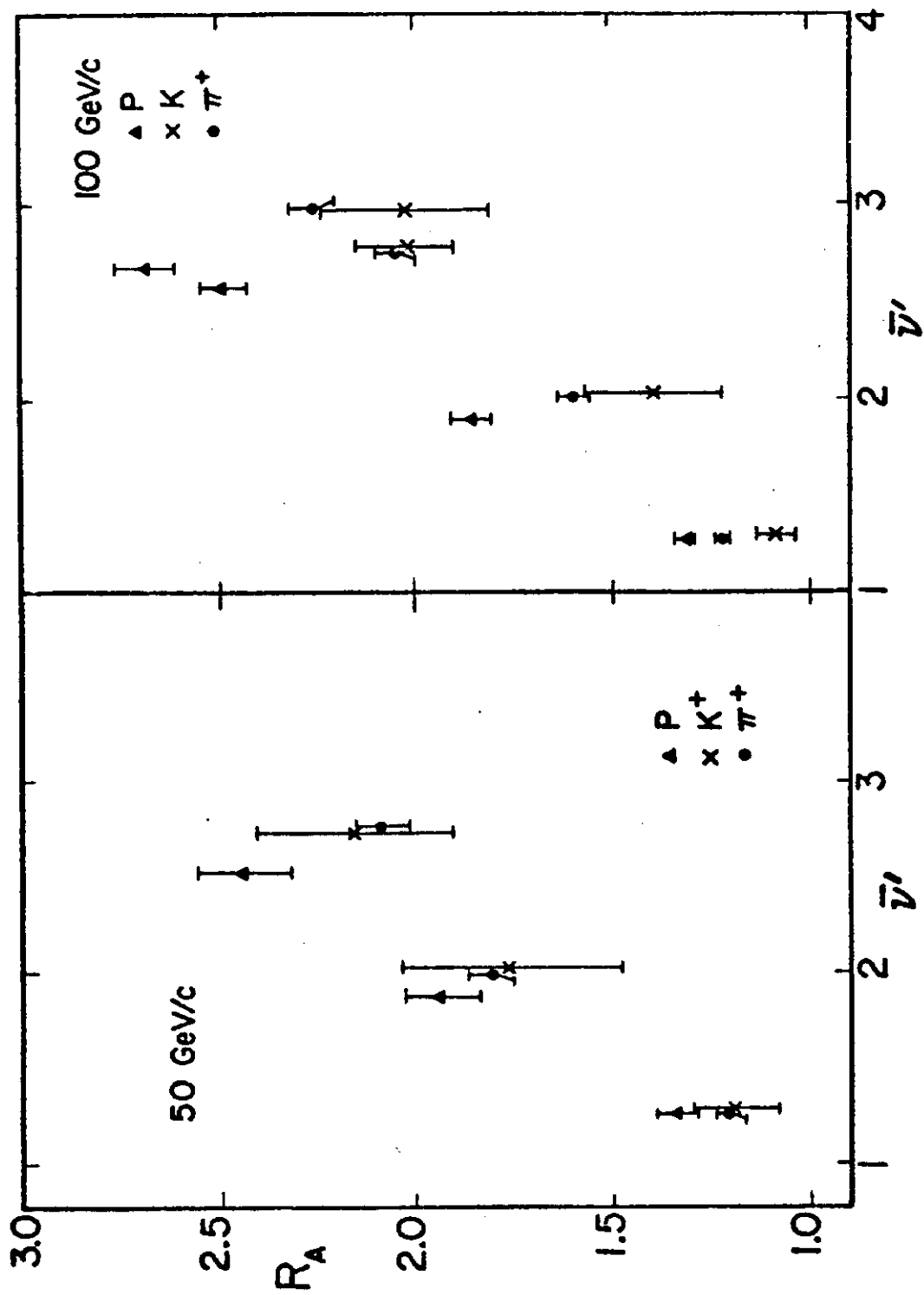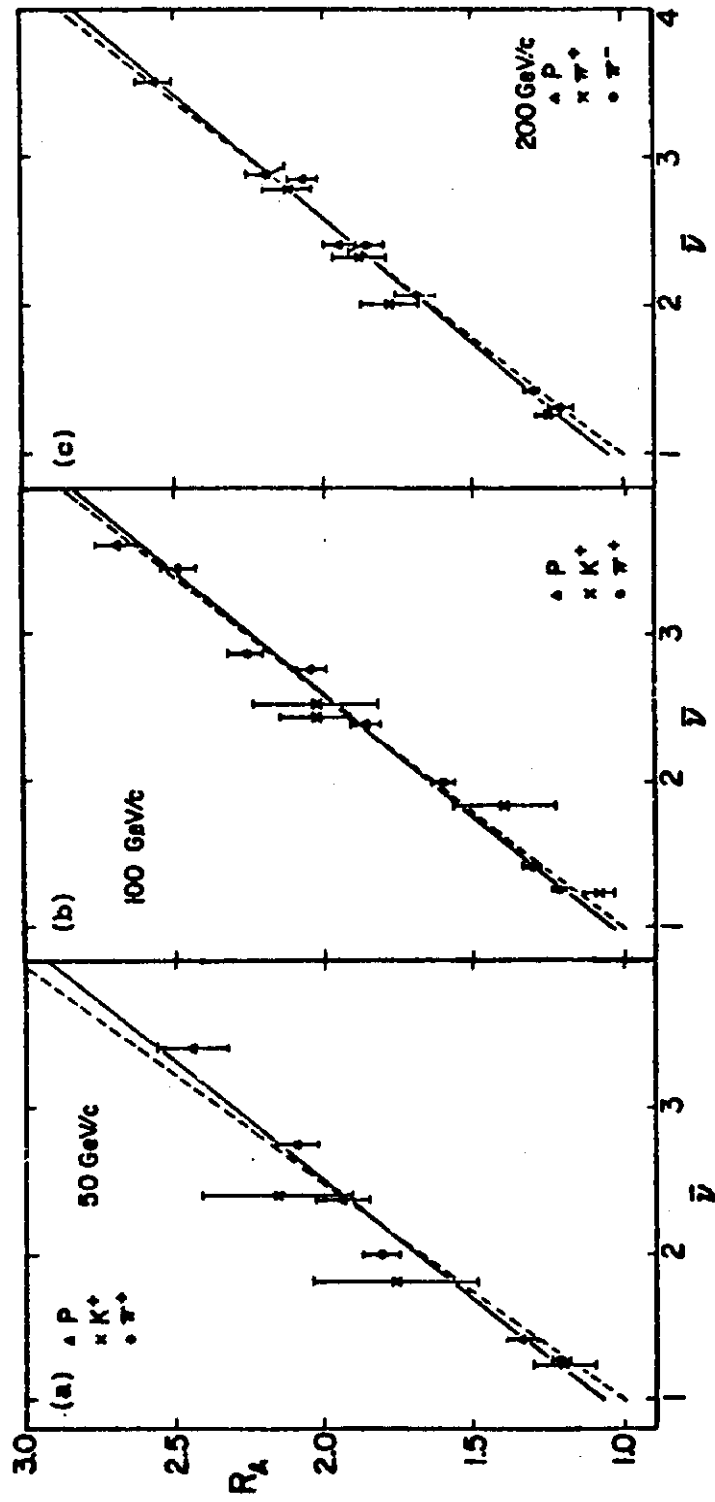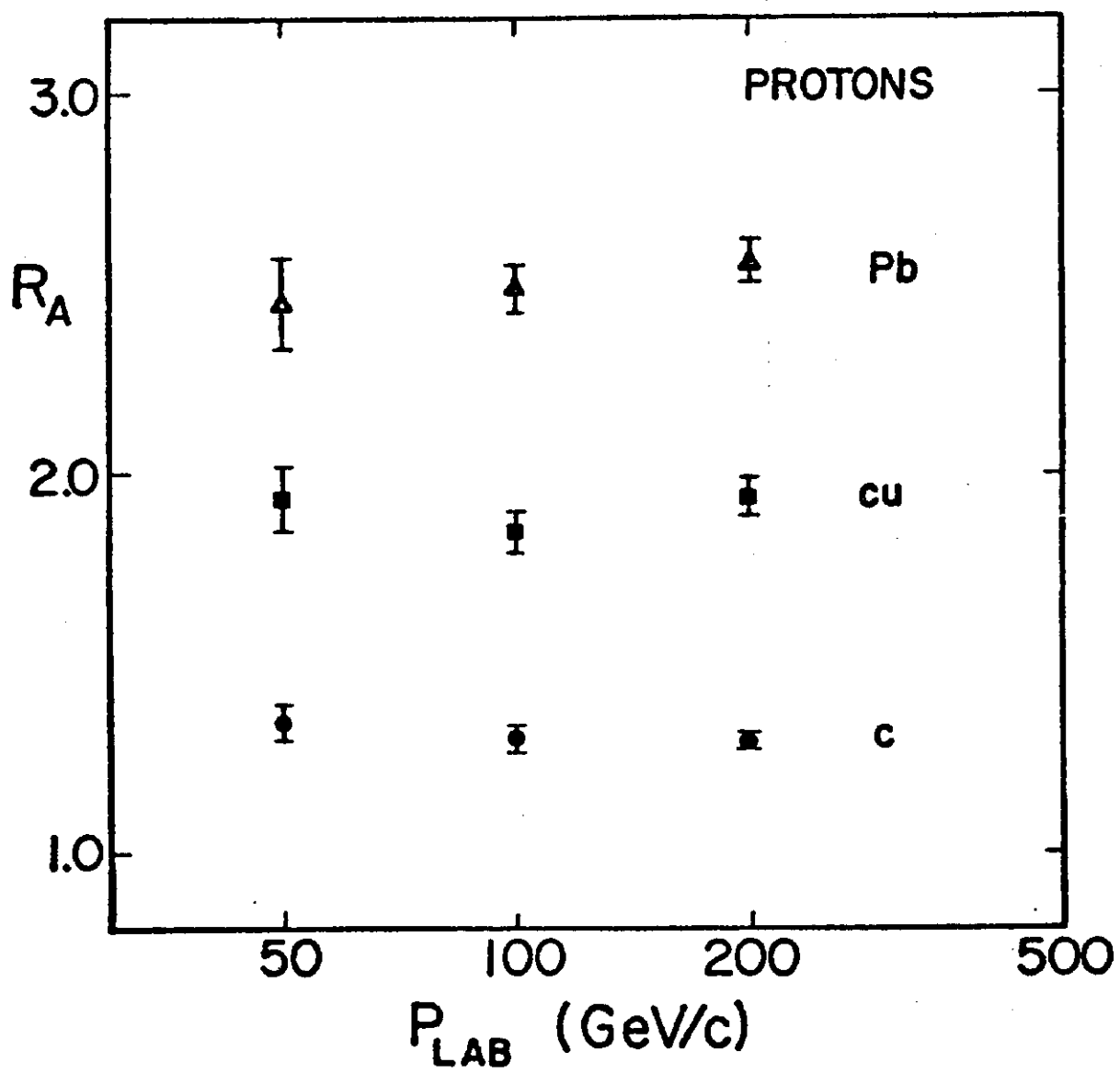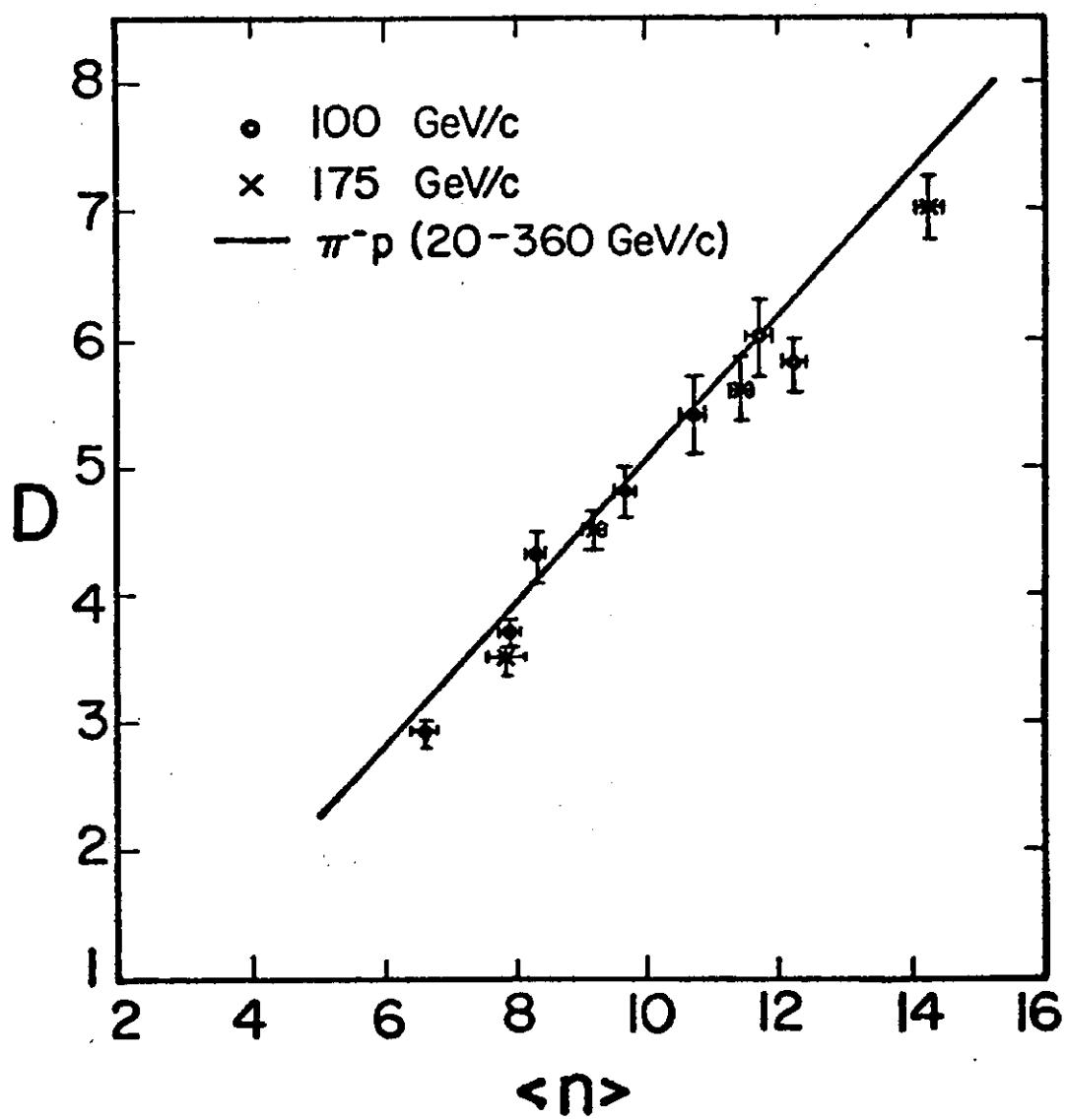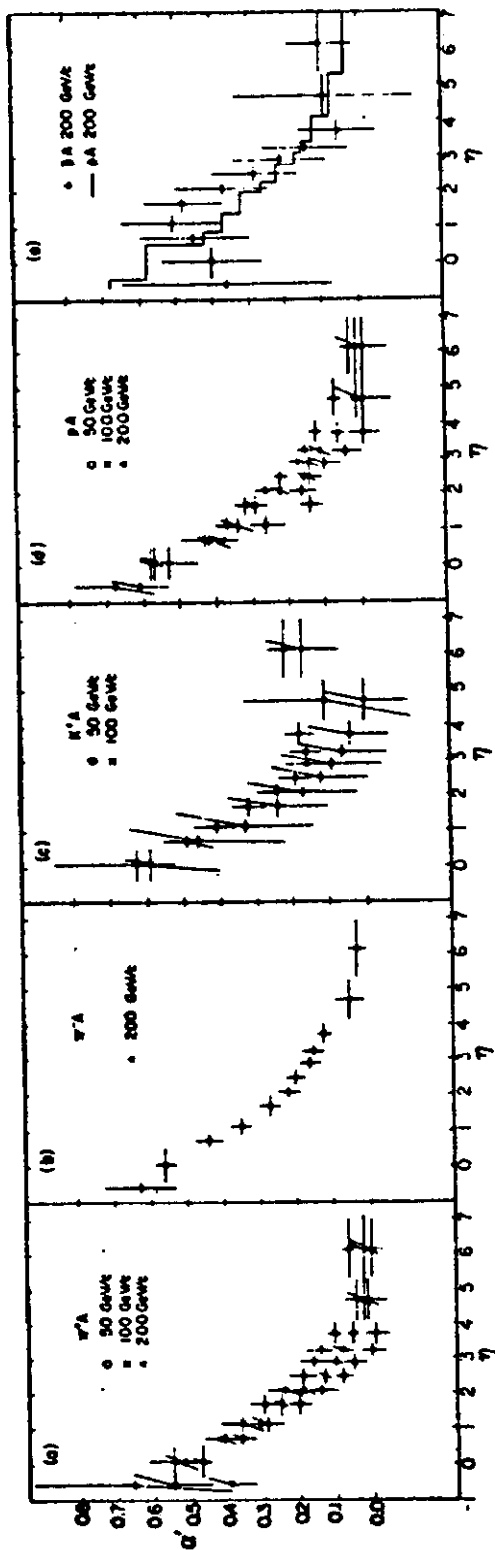
Fig. 5.
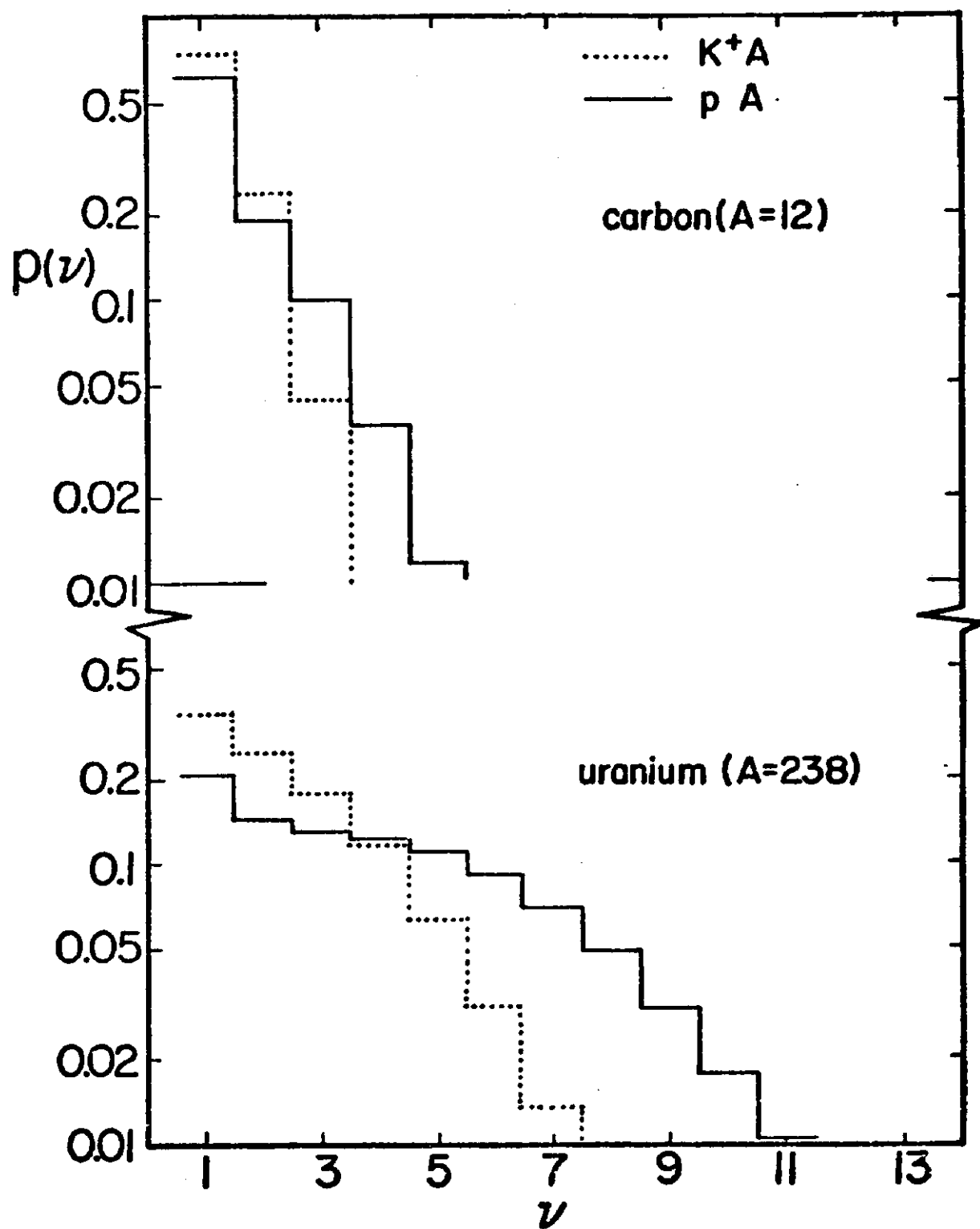
Fig. 6.
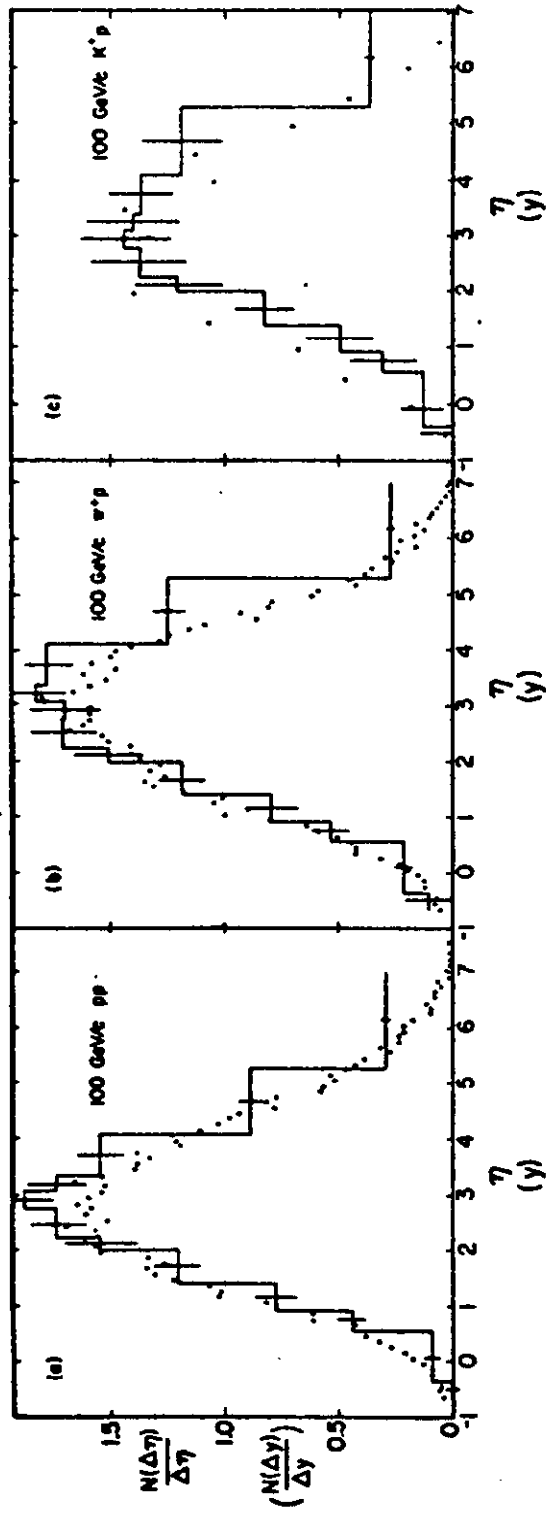
Fig. 7.
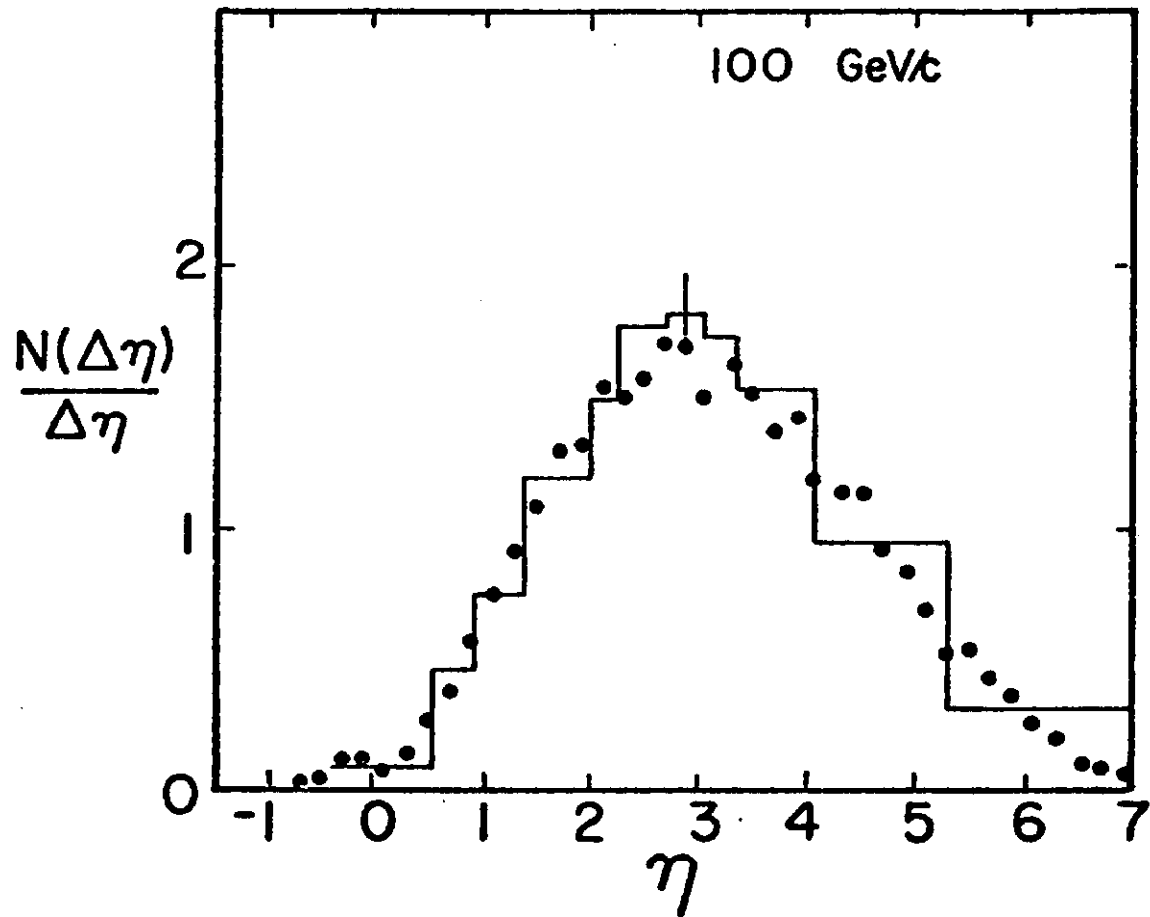
Fig. 8.
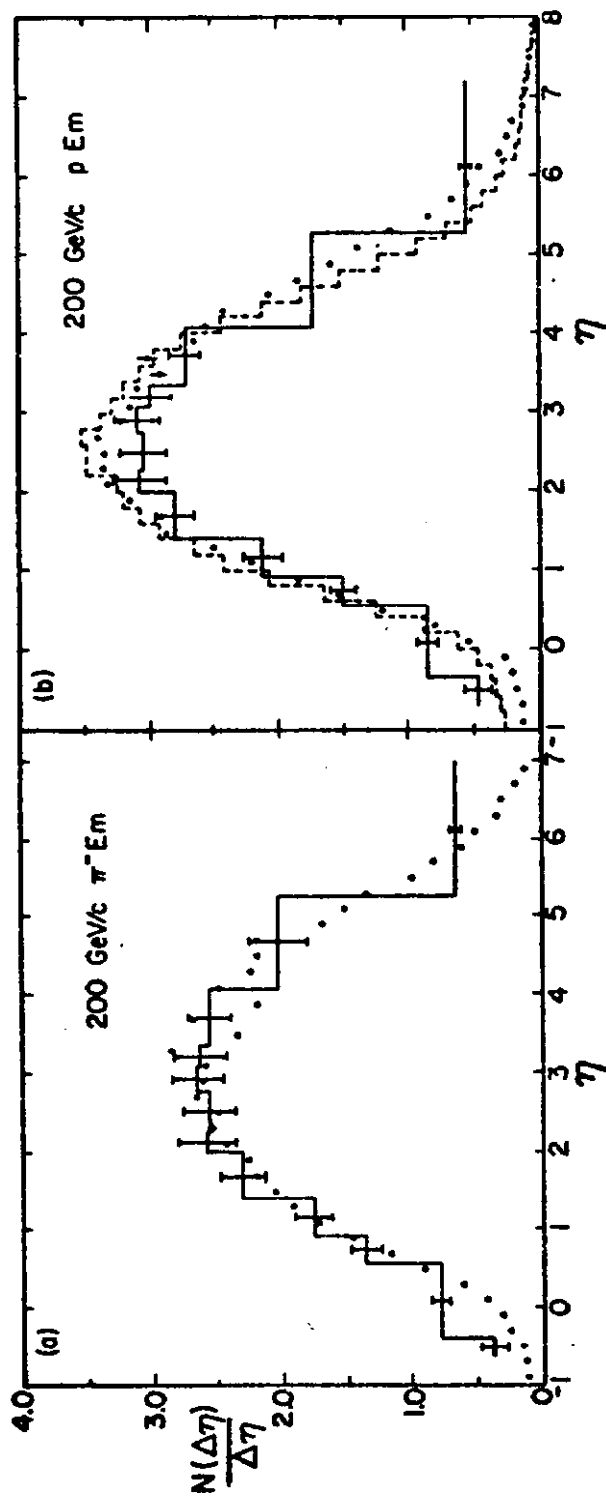
Fig. 9.
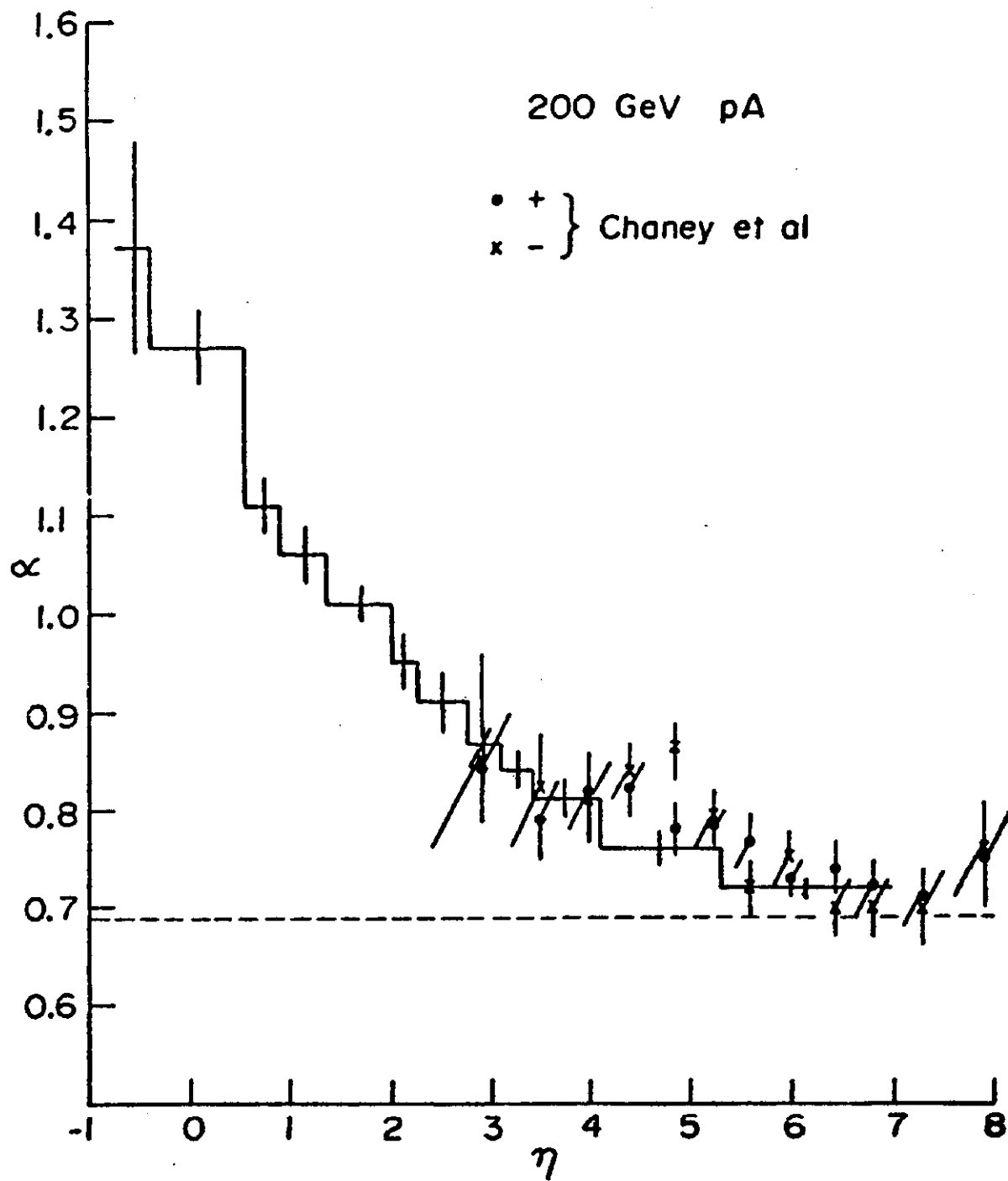
Fig. 10.
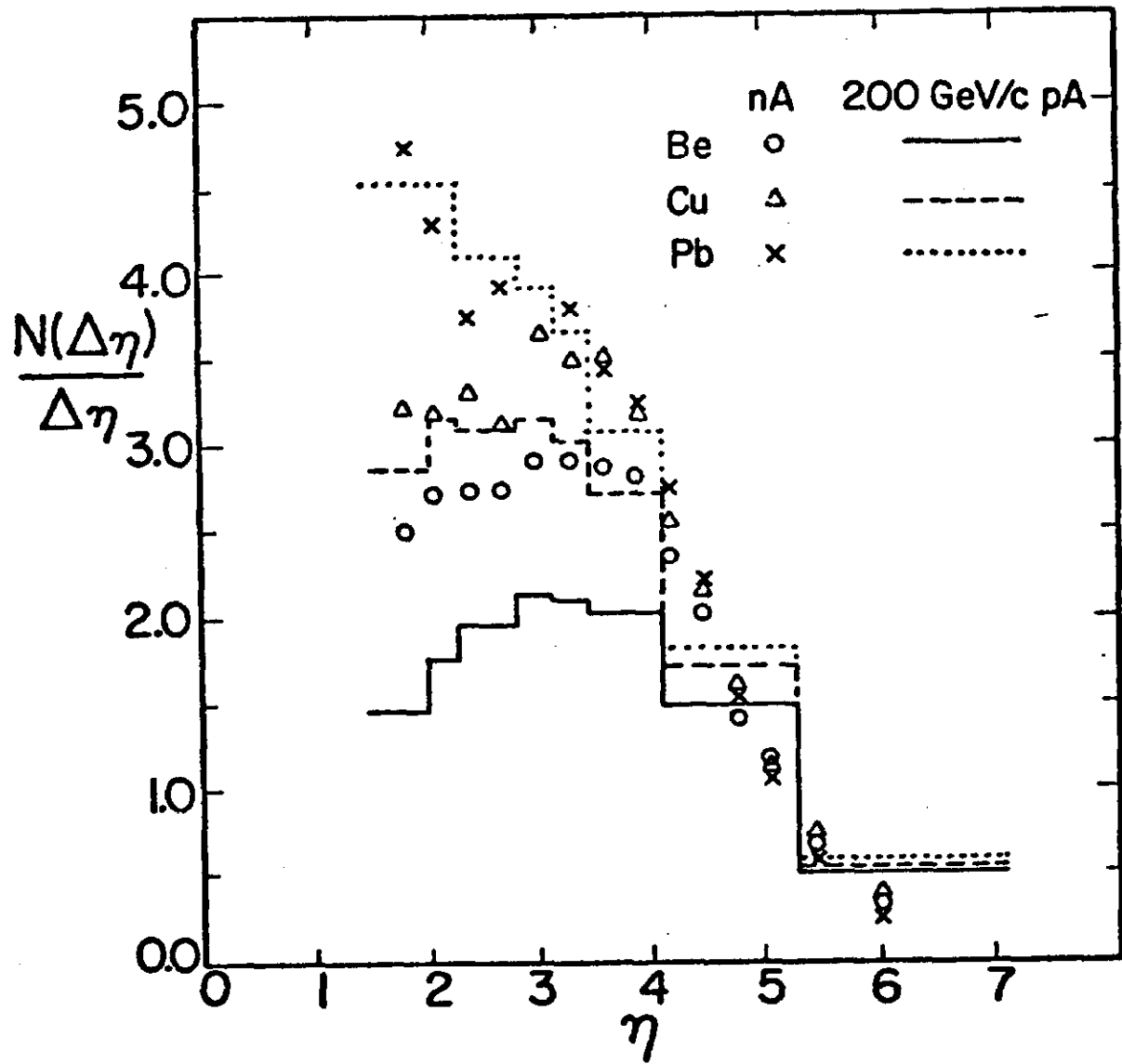
Fig. 11.
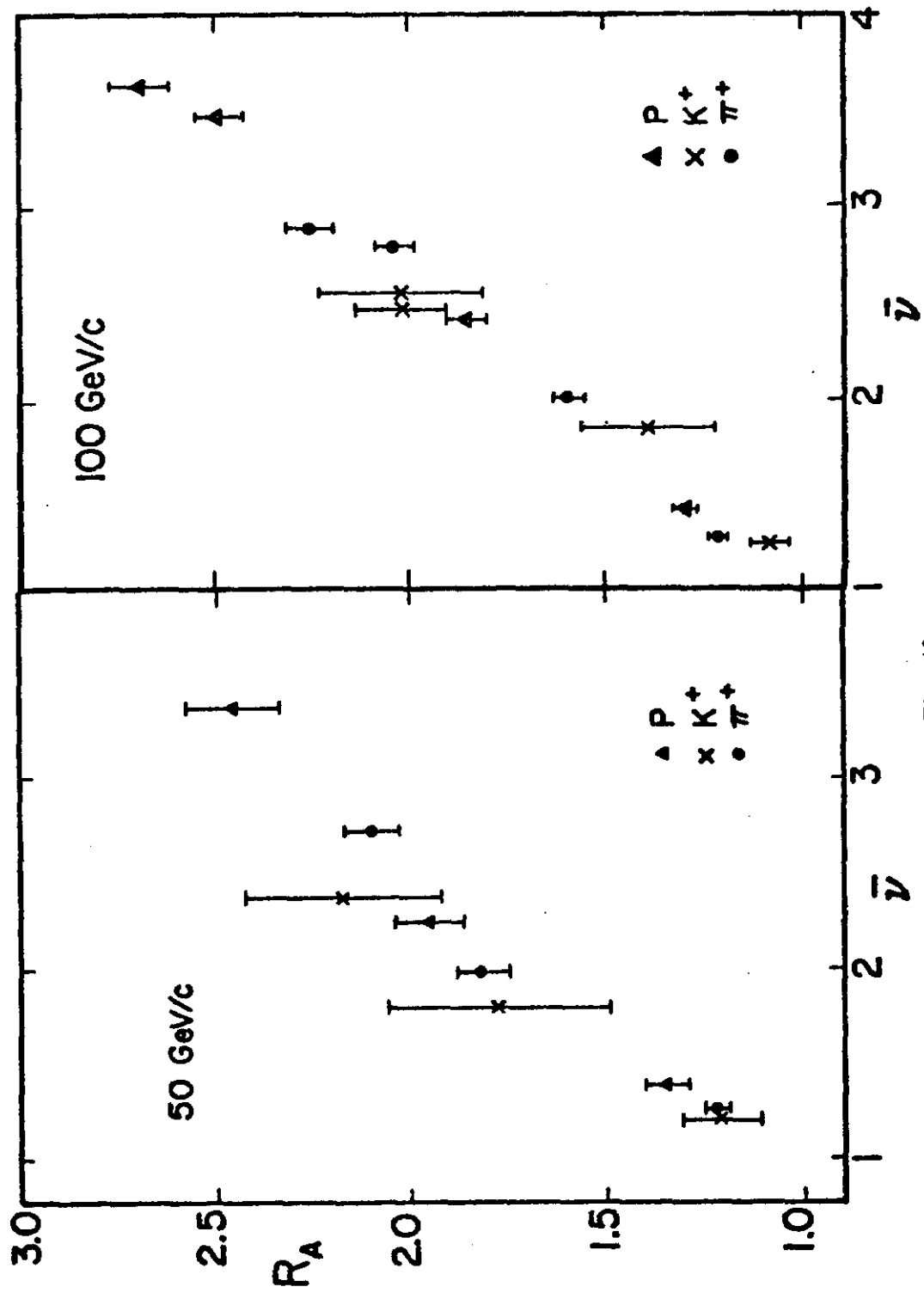
Fig. 12.

Fig. 13.

Fig. 14.

Fig. 15.

Fig. 16.

Fig. 17.
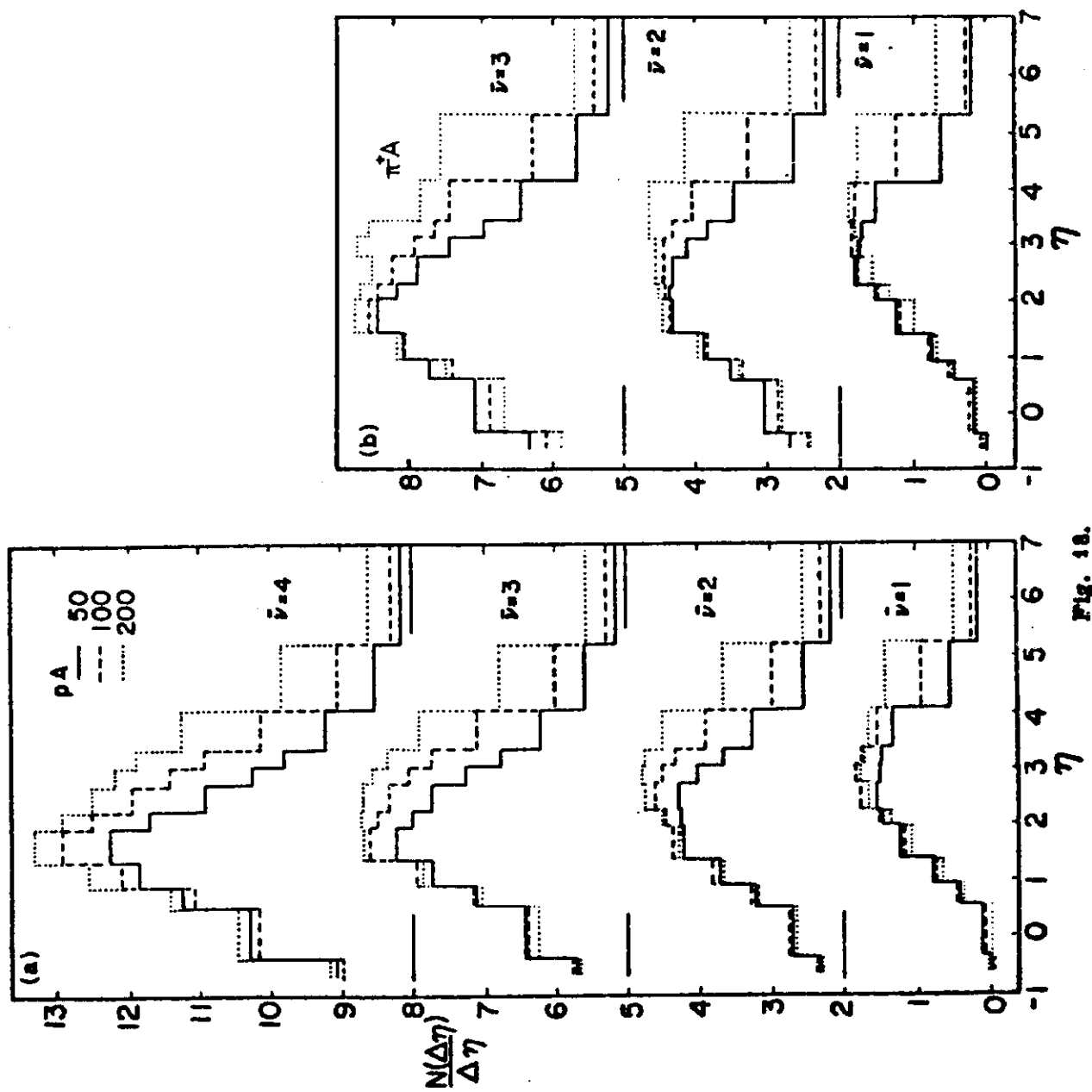
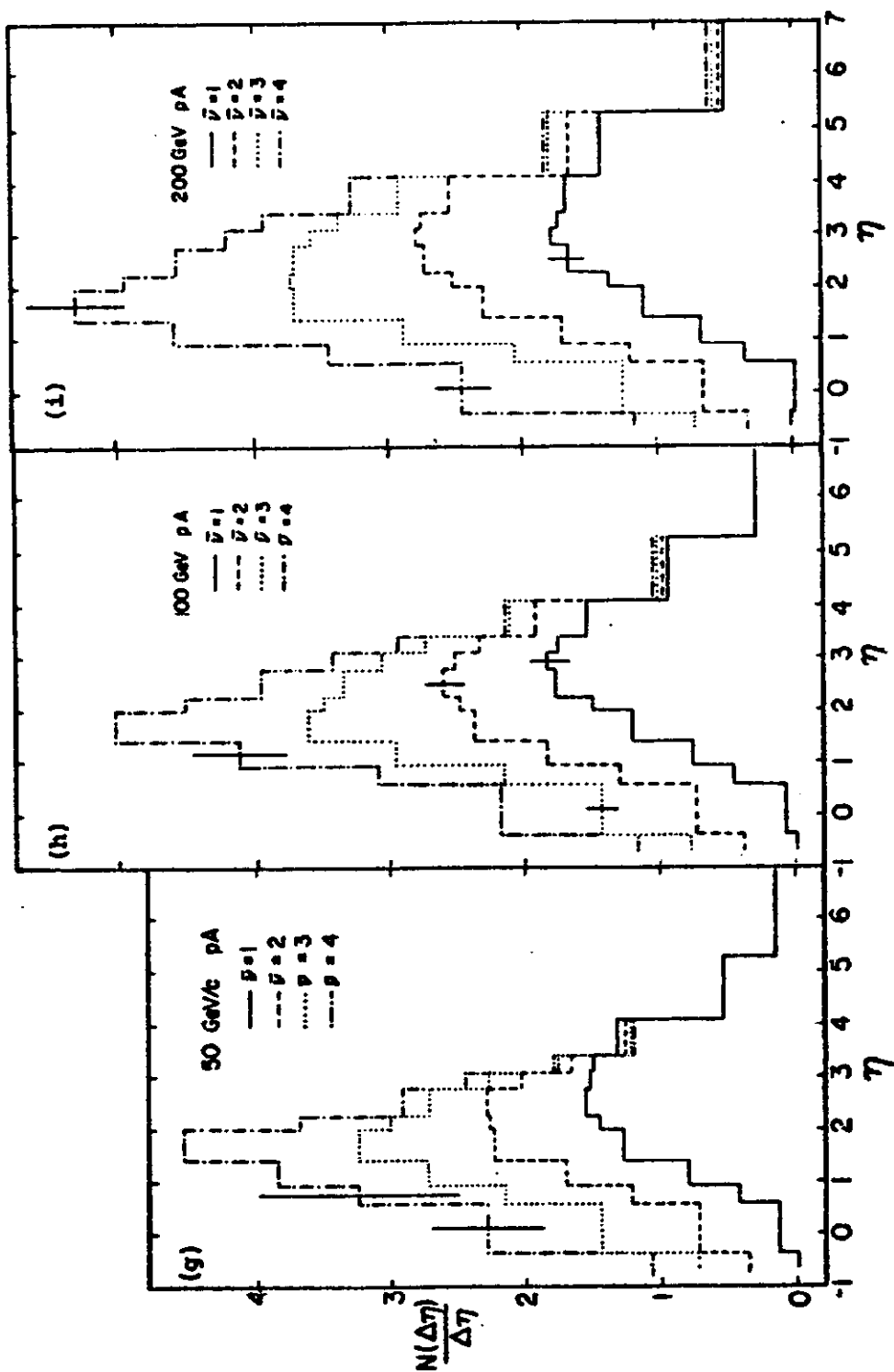Fig. 18.
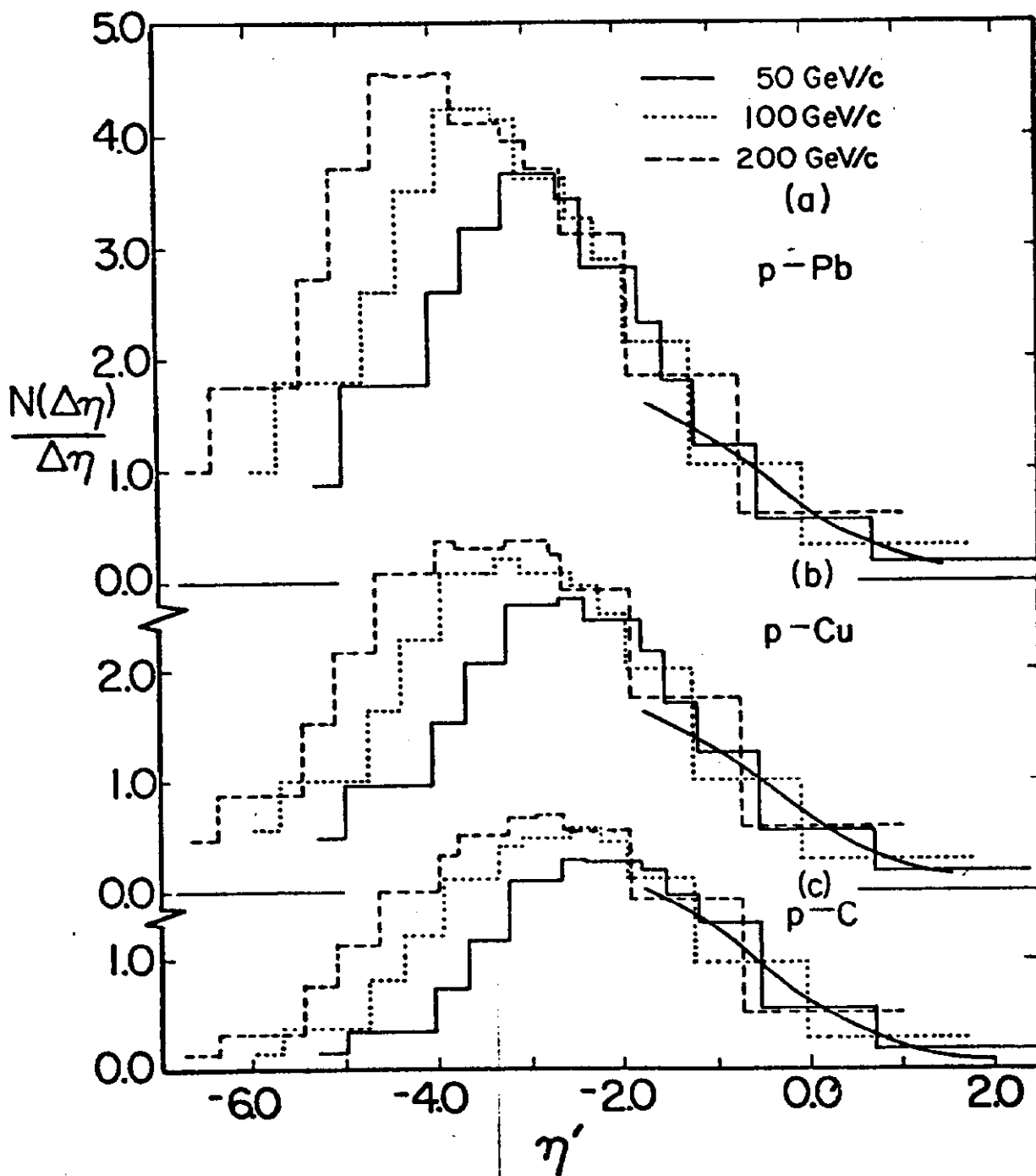
Fig. 19.
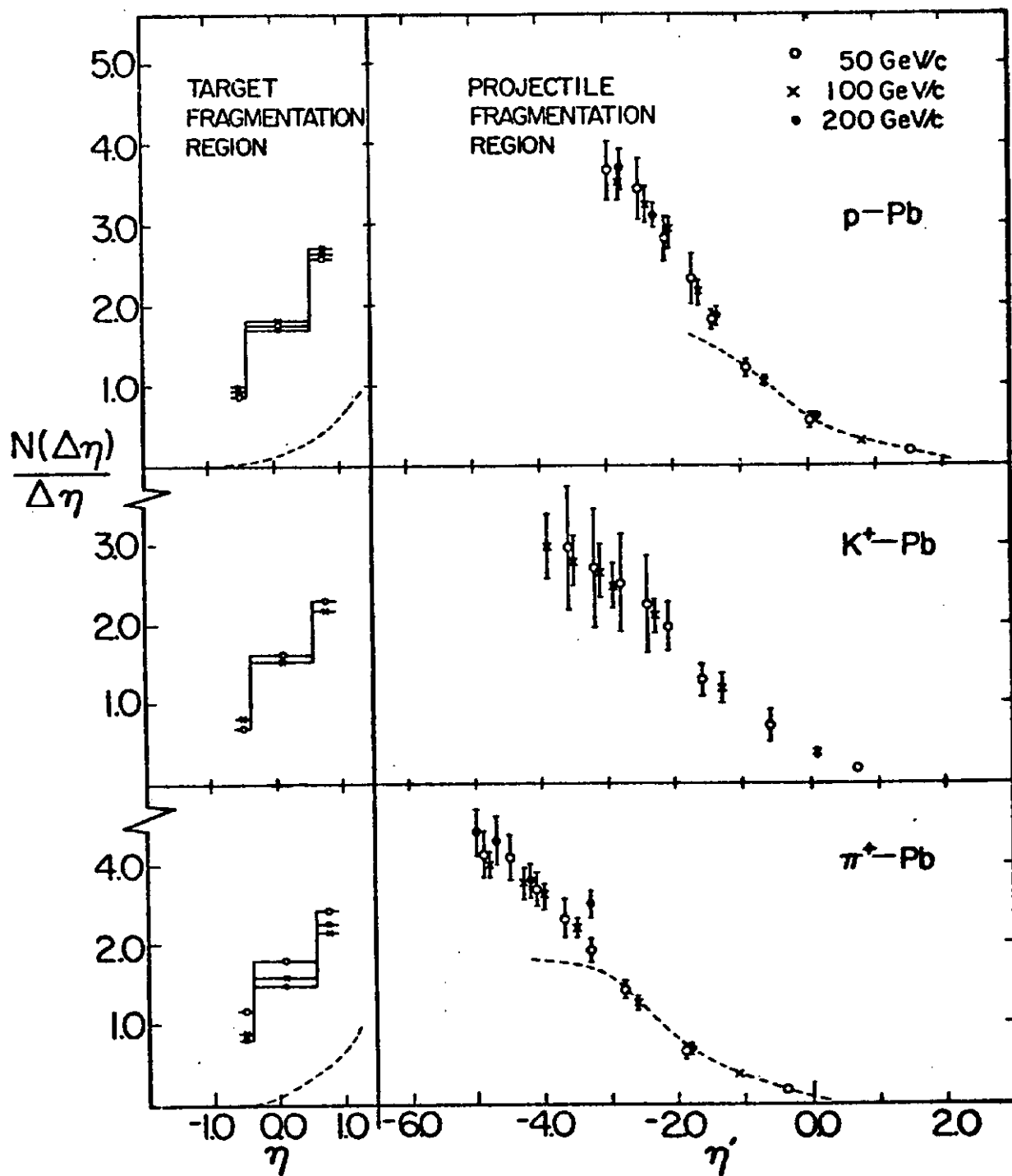
Fig. 20.

Fig. 22 (a), (b), (c), (d).
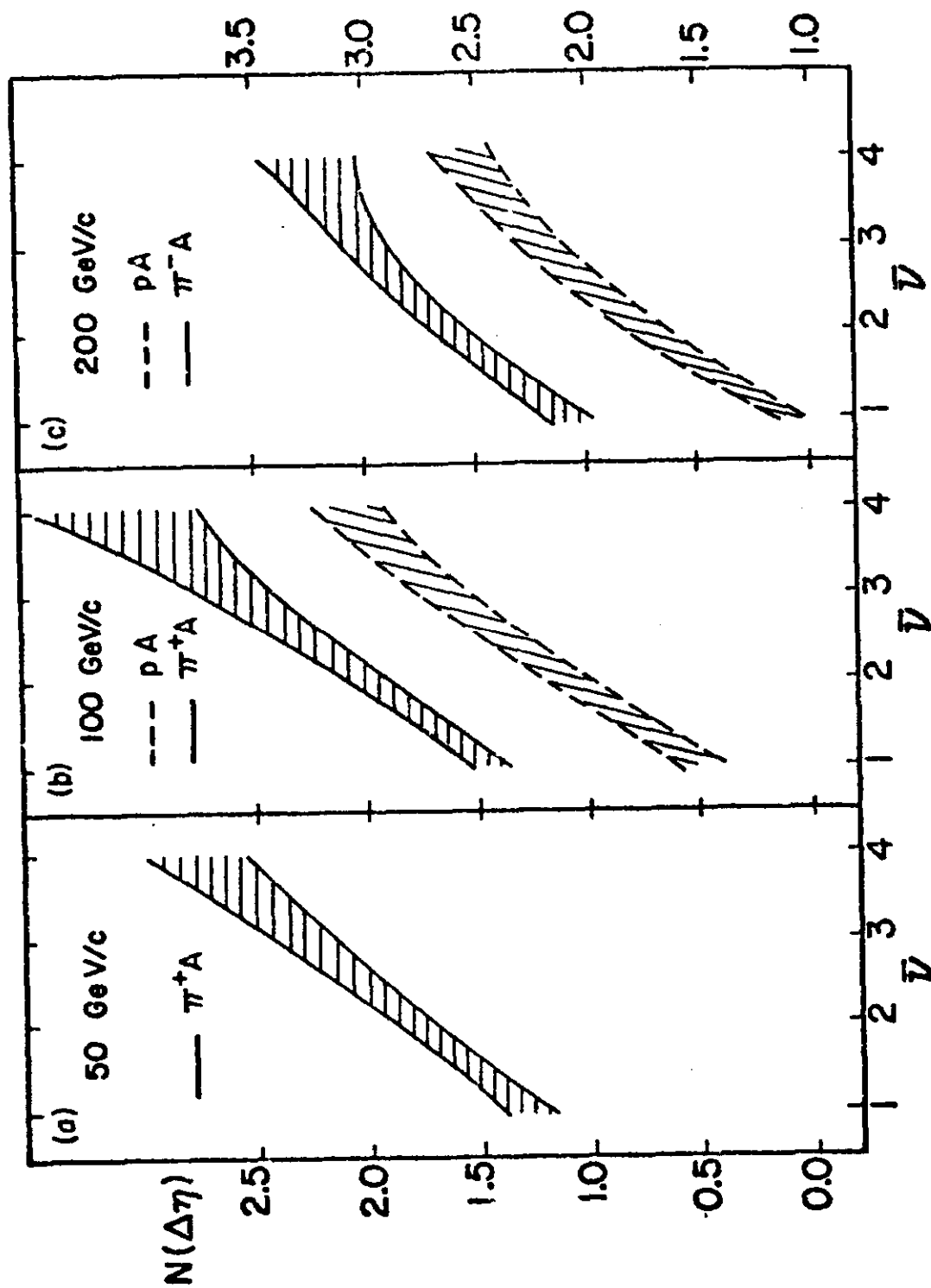
Fig. 21.

Fig. 22(e), (f).

Fig. 22. (g), (h), (i).

Fig. 23.